Article

Cell Metabolism

A Stat6/Pten Axis Links Regulatory T Cells with Adipose Tissue Function

Graphical Abstract

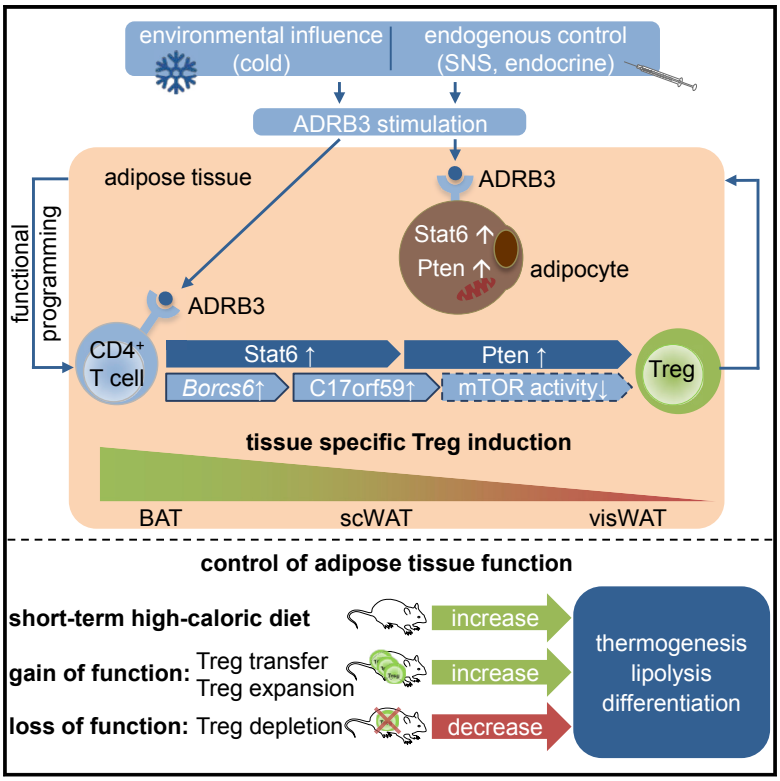

Highlights

- Cold exposure or beta3-adrenergic stimuli induce adipose tissue Foxp3$^+$ Tregs
- Short-term high-calorie diet induces Foxp3$^+$ Tregs in brown adipose tissue
- Stat6 links Foxp3$^+$ Tregs with adipose tissue function
- Cold exposure or beta3-adrenergic stimulation increases C17orf59 expression

Authors

Stefanie Kälin, Maike Becker, Verena B. Ott, ..., Matthias Mann, Matthias H. Tschöp, Carolin Daniel

Correspondence

tschoep@helmholtz-muenchen.de (M.H.T.), carolin.daniel@helmholtz-muenchen.de (C.D.)

In Brief

Obesity and type 2 diabetes are associated with metabolic defects and adipose tissue inflammation. Kälin et al. report that a T cell-specific Stat6/Pten signaling axis links cold exposure or adrenergic stimuli with immunosuppressive regulatory T cell activity and adipose tissue function, offering novel molecular targets for improvement of adipose tissue function.

Data Resources

PXD004671

Kälin et al., 2017, Cell Metabolism *26*, 475–492
September 5, 2017
http://dx.doi.org/10.1016/j.cmet.2017.08.008

Cell Metabolism
Article

A Stat6/Pten Axis Links Regulatory T Cells with Adipose Tissue Function

Stefanie Kälin,[1,2,17] Maike Becker,[2,3,17] Verena B. Ott,[1,2,4] Isabelle Serr,[2,3] Fabian Hosp,[5] Mohammad M.H. Mollah,[2,3] Susanne Keipert,[1,2] Daniel Lamp,[1,2] Francoise Rohner-Jeanrenaud,[6] Victoria K. Flynn,[2,3] Martin G. Scherm,[2,3] Lucas F.R. Nascimento,[2,3] Katharina Gerlach,[7] Vanessa Popp,[7] Sarah Dietzen,[8] Tobias Bopp,[8] Purna Krishnamurthy,[9] Mark H. Kaplan,[9] Manuel Serrano,[10] Stephen C. Woods,[11] Philipp Tripal,[12] Ralf Palmisano,[12] Martin Jastroch,[1,2] Matthias Blüher,[13] Christian Wolfrum,[14] Benno Weigmann,[7] Anette-Gabriele Ziegler,[2,15,16] Matthias Mann,[5] Matthias H. Tschöp,[1,2,18,*] and Carolin Daniel[3,2,*]

[1]Institute for Diabetes and Obesity, Helmholtz Diabetes Center at Helmholtz Zentrum München and Division of Metabolic Diseases, Department of Medicine, Technische Universität München, 85748 Munich, Germany
[2]German Center for Diabetes Research (DZD), 85764 Munich-Neuherberg, Germany
[3]Institute for Diabetes Research, Research Group Immune Tolerance in Diabetes, Helmholtz Diabetes Center at Helmholtz Zentrum München, 80939 Munich, Germany
[4]Institute for Advanced Study, Technische Universität München, 85748 Garching, Germany
[5]Max Planck Institute of Biochemistry, 82152 Martinsried, Germany
[6]Laboratory of Metabolism, Division of Endocrinology, Diabetology, Hypertension, and Nutrition, Department of Internal Medicine Specialties, Faculty of Medicine, University of Geneva, Geneva, Switzerland
[7]Department of Medicine 1, University of Erlangen-Nuremberg, 91052 Erlangen, Germany
[8]Institute of Immunology, University Medical Center of the Johannes Gutenberg University, 55131 Mainz, Germany
[9]Department of Pediatrics and HB Wells Center for Pediatric Research, Indiana University School of Medicine, Indianapolis, IN 46202, USA
[10]Tumour Suppression Group, Spanish National Cancer Research Centre (CNIO), 28029 Madrid, Spain
[11]Department of Psychiatry and Behavioral Neuroscience, University of Cincinnati, Cincinnati, OH, USA
[12]OICE (Optical Imaging Centre Erlangen), University Erlangen, 91052 Erlangen, Germany
[13]Department of Medicine, Research Group Molecular Endocrinology, University of Leipzig, 04103 Leipzig, Germany
[14]Swiss Federal Institute of Technology, Institute of Food Nutrition and Health, Laboratory of Translational Nutrition Biology, ETH Zurich, 8603 Schwerzenbach, Switzerland
[15]Institute for Diabetes Research, Helmholtz Diabetes Center at Helmholtz Zentrum München, 80939 Munich, Germany
[16]Klinikum rechts der Isar, Technische Universität München, 80333 Munich, Germany
[17]These authors contributed equally
[18]Lead Contact
*Correspondence: tschoep@helmholtz-muenchen.de (M.H.T.), carolin.daniel@helmholtz-muenchen.de (C.D.)
http://dx.doi.org/10.1016/j.cmet.2017.08.008

SUMMARY

Obesity and type 2 diabetes are associated with metabolic defects and adipose tissue inflammation. Foxp3$^+$ regulatory T cells (Tregs) control tissue homeostasis by counteracting local inflammation. However, if and how T cells interlink environmental influences with adipocyte function remains unknown. Here, we report that enhancing sympathetic tone by cold exposure, beta3-adrenergic receptor (ADRB3) stimulation or a short-term high-calorie diet enhances Treg induction *in vitro* and *in vivo*. CD4$^+$ T cell proteomes revealed higher expression of Foxp3 regulatory networks in response to cold or ADRB3 stimulation *in vivo* reflecting Treg induction. Specifically, Ragulator-interacting protein C17orf59, which limits mTORC1 activity, was upregulated in CD4$^+$ T cells by either ADRB3 stimulation or cold exposure, suggesting contribution to Treg induction. By loss- and gain-of-function studies, including Treg depletion and transfers *in vivo*, we demonstrated that a T cell-specific Stat6/Pten axis links cold exposure or ADRB3 stimulation with Foxp3$^+$ Treg induction and adipose tissue function. Our findings offer a new mechanistic model in which tissue-specific Tregs maintain adipose tissue function.

INTRODUCTION

Obesity and type 2 diabetes (T2D) are among the most severe health threats of modern society. Each of these metabolic disorders is associated with tissue-specific maladaptive alterations, including amplified inflammatory processes in individual fat depots. Based on the currently accepted model, adipocytes can be divided into classes of white, brown, and beige cells (Rosen and Spiegelman, 2014) and are surrounded by several immune cell types. Immune cell type composition, number, and function dramatically change in visceral white adipose tissue (visWAT) in response to overnutrition. Accordingly, visWAT is especially prone to obesity-associated inflammation (Rosen and Spiegelman, 2014).

CD4$^+$CD25$^+$Foxp3$^+$ regulatory T cells (Tregs) critically contribute to tissue homeostasis by interfering with local inflammation. Tregs can be induced in the peripheral immune system,

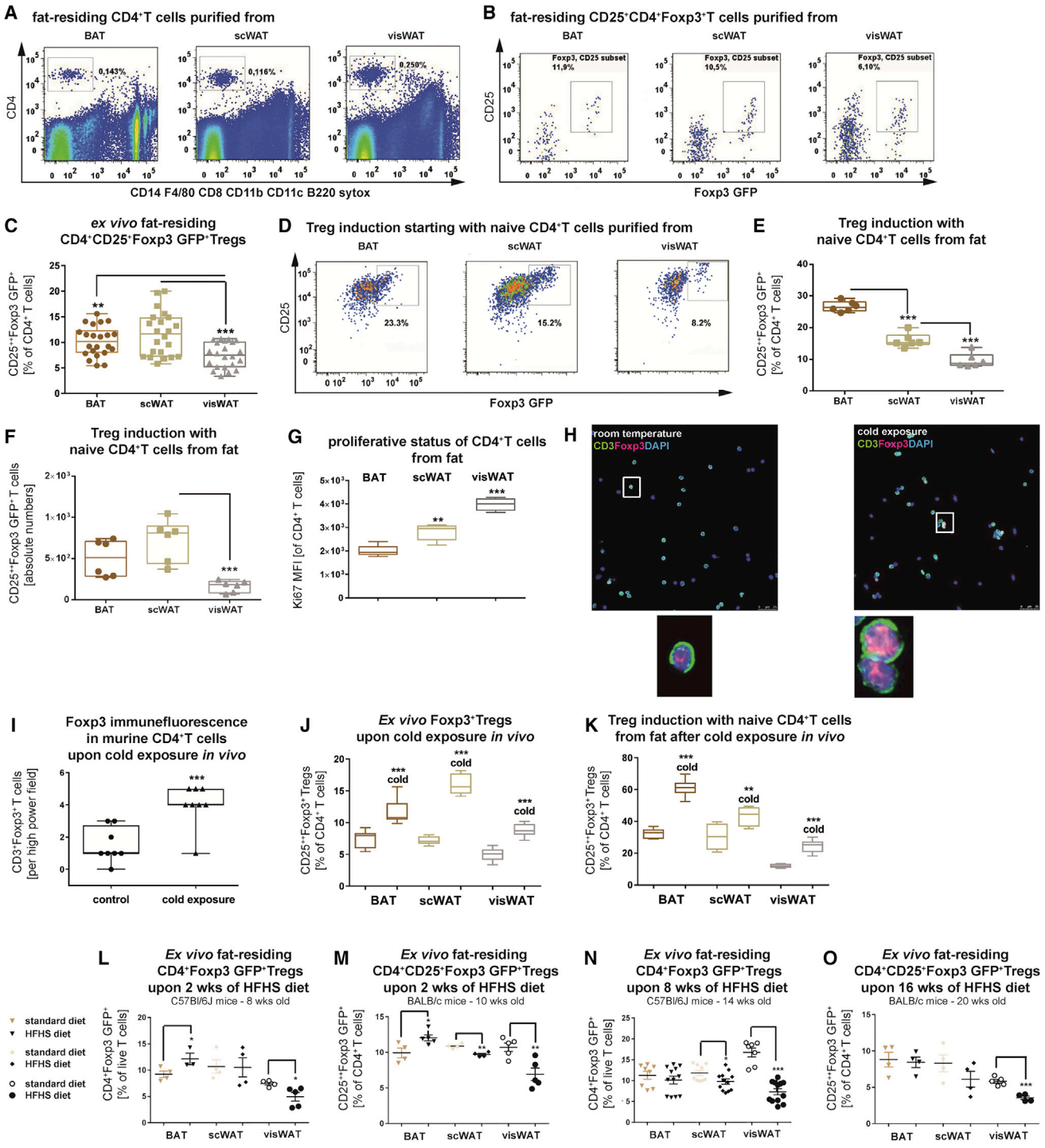

Figure 1. Treg Accumulation in Brown and White Adipose Tissue

(A) Representative fluorescence-activated cell sorting (FACS) plots for identification of fat-residing CD4$^+$ T cells from BAT, scWAT, or visWAT of young lean female BALB/c Foxp3GFP reporter mice. CD4$^+$ T cells were gated on CD14$^-$, F4/80$^-$, CD8a$^-$, CD11b$^-$, CD11c$^-$, B220, and sytox$^-$.

(B) Representative FACS plots for identification of fat-residing CD4$^+$CD25^{++}Foxp3GFP$^+$ Tregs in BAT, scWAT, or visWAT. Plots are pre-gated as shown in (A).

(C) Box-and-whisker plots for frequencies of CD25$^+$Foxp3GFP$^+$ Tregs residing in fat depots as indicated in (B). n = 22 per group from five independent experiments.

(D) Representative FACS plots for *in vitro* Treg induction assays using limited TCR stimulation and naive CD4$^+$ T cells purified from fat depots.

(E and F) *In vitro* Treg induction assays of fat-residing CD4$^+$ T cells (E) and absolute Treg numbers (F) obtained starting with identical numbers of naive CD4$^+$ T cells. n = 6 per group.

(G) Summary graph for proliferating CD4$^+$ T cells from fat depots as assessed by Ki67 mean fluorescence intensity (MFI). n = 5 per group.

(legend continued on next page)

a process referred to as Treg induction (von Boehmer and Daniel, 2013).

Recently, a critical function of fat-residing $CD4^+$ T effector and Tregs in adipose-immune crosstalk was reported (Bapat et al., 2015; Cipolletta et al., 2012; Feuerer et al., 2009). Specifically, a subcategory of Tregs was identified as functionally participating in maintenance of visWAT energy homeostasis (Cipolletta et al., 2012; Feuerer et al., 2009; Mathis, 2013). Functional orchestration of Treg populations in visWAT is influenced by PPAR-γ signaling (Cipolletta et al., 2012; Panduro et al., 2016); i.e., PPAR-γ collaborates with Foxp3 to impose the transcriptional profile characteristic of visWAT Tregs onto naive $CD4^+$ T cells (Cipolletta et al., 2012). Fat-residing Tregs control local inflammatory processes.

However, despite these insights in adipose-immune crosstalk in visWAT, including the contribution of Treg cells, our understanding of Treg function and the subsequent interaction with subcutaneous white adipose tissue (scWAT) and brown adipose tissue (BAT) remains in its infancy. One relevant study reported that Tregs in BAT of female C57BL/6 mice have a different transcriptome than that of their splenic counterparts (Medrikova et al., 2015).

In addition, the molecular underpinnings of the functional interplay between adipose tissue (AT) and Treg cells, especially in scWAT and BAT, remain largely unknown, and we hypothesized that this Treg-adipose crosstalk is at least partially regulated by environmental influences. However, if and how T cells and Tregs interlink environmental challenges with adipocyte function are still unclear. Specific insights into the mutual crosstalk between local Tregs and AT, especially in BAT and scWAT, are critical for the development of precision interventions to improve and maintain AT function.

To mechanistically dissect Treg induction in adipose function, we focused on three environmental influences to increase sympathetic tone *in vivo*: cold exposure and enhancement of sympathetic tone (beta3-adrenergic signaling) as well as on short-term exposure to a high-caloric challenge as a means of inducing diet-induced thermogenesis. Cold exposure was chosen based on its major role in the regulation of energy expenditure and consequent significant impact on diverse metabolic processes of AT, especially as recent studies uncovered cold-inducible BAT in adult humans (Cypess et al., 2013; Saito et al., 2009). Accordingly, cold exposure or short-term cryostimulation was used to activate beta3-adrenergic receptors (ADRB3s) in clinical situations; e.g., in rheumatoid arthritis or multiple sclerosis (Guillot et al., 2014). Further, increased anti-inflammatory cytokine production has been reported upon short-term cryostimulation (Klimek et al., 2011; Lubkowska et al., 2011), and short-term high-calorie exposure supports BAT thermogenesis (Rothwell and Stock, 1979).

Here, we report that cold exposure or ADRB3 stimulation induces Tregs *in vitro* as well as *in vivo*. Diet-induced thermogenesis likewise increased $Foxp3^+$ Treg numbers and their induction in BAT. Mechanistically, using $CD4^+$ T cell proteomes, we uncovered Treg induction and higher protein expression of Foxp3 regulatory networks. Specifically, the Ragulator-interacting protein C17orf59, which limits mTORC1 activity, was upregulated by both ADRB3 stimulation and cold exposure, likely supporting enhanced Treg induction. Using a series of T cell-specific and adipose-related loss- and gain-of-function studies, including depletion, transfers, and expansion of Tregs *in vivo*, we demonstrated that a T cell-specific Stat6/Pten axis adjusts $Foxp3^+$ Treg induction and AT function according to the degree of sympathetic tone and environmental temperature.

RESULTS

BAT and scWAT Harbor Higher $Foxp3^+$ Treg Percentages than visWAT

To dissect the interplay between the induction of Tregs and adipose function, we first investigated their frequency, functional characteristics, and induction in different fat depots using young lean BALB/c Foxp3 GFP reporter mice (3–6 weeks of age). A set of exclusion markers permitted the direct identification of a $CD4^+$ T cell subset purified from three fat depots (Figure 1A). Locally residing $CD4^+CD25^+Foxp3GFP^+$ Treg percentages were higher in BAT and scWAT than in visWAT (Tregs in BAT versus visWAT, $p = 0.0015$; Tregs in scWAT versus visWAT, $p = 0.0003$; Figures 1B and 1C).

Treg Induction Is More Efficient in T Cells from BAT and scWAT than from visWAT

To determine $Foxp3^+$ Treg induction capacities in different fat depots, we purified naive $CD4^+CD25^-Foxp3GFP^-CD44^{low}$ T cells from BAT, scWAT, and visWAT of BALB/c Foxp3-GFP reporter mice. We based our approach on recently emerging evidence that naive $CD4^+CD25^-$ T cells are present in various non-lymphoid tissues (Kim, 2007; Lewis et al., 2008). Efficient $Foxp3^+$ Treg induction requires subimmunogenic stimulation of naive $CD4^+$ T cells (Daniel and von Boehmer, 2011; Daniel et al., 2011; Gottschalk et al., 2010), while a lower proliferative capacity of T cells results in more efficient Treg induction (Kretschmer et al., 2005). To mimic such subimmunogenic T cell receptor (TCR) stimulation *in vitro*, we used premature withdrawal of TCR stimulation in the absence of transforming growth factor β (Sauer et al., 2008; Serr et al., 2016).

(H) Representative confocal microscopy images of $CD4^+$ T cells purified from mice upon *in vivo* cold exposure (4 days, 8°C). Scale bar, 25 μm.
(I) $Foxp3^+CD3^+$ T cells per high power field in samples from (G). n = 8 per group from SEM from two independent experiments.
(J) *Ex vivo* Treg frequencies purified from AT of young BALB/c mice upon *in vivo* cold exposure (24 hr, 4°C). n = 9 per group.
(K) *In vitro* Treg induction assays of fat-residing naive $CD4^+$ T cells after *in vivo* cold exposure (24 hr, 4°C). n = 6 per group.
(L and M) *Ex vivo* $CD4^+CD25^{++}Foxp3^+$ Treg frequencies in fat depots of 8-week-old C57BL/6J mice (L) or 10-week-old BALB/c mice (M) that were subjected to 2 weeks of HFHS diet. n = 4 per group in (L), n > 4 per group in (M).
(N) Summary graphs for *ex vivo* $CD4^+CD25^{++}Foxp3^+$ Treg frequencies in BAT, scWAT, and visWAT of 14-week-old C57BL/6J mice upon 8 weeks of HFHS diet. n = 12 for HFHS diet group, n = 8 for standard diet group.
(O) Depicted are *ex vivo* fat-residing $CD4^+CD25^{++}Foxp3^+$ Tregs of 20-week-old BALB/c animals that were on an HFHS diet for 16 weeks. n = 4–5 per group.
See also Figure S1. Data are presented as box-and-whisker plots with min and max values for data distribution or as means ± SEM. *p < 0.05, **p < 0.01, ***p < 0.001.

Specifically, we compared Treg induction between naive $CD4^+CD25^-Foxp3GFP^-CD44^{low}$ T cells from different fat depots. Treg induction was most efficient using naive T cells purified from BAT and scWAT (induced $CD4^+CD25^{++}Foxp3^+$ Tregs [% of $CD4^+$ T cells] BAT 26.5 ± 0.6 versus scWAT 16.0 ± 0.9; Figures 1D–1F). Significantly lower induced Treg frequencies were obtained with naive $CD4^+$ T cells from visWAT (induced $CD4^+CD25^{++}Foxp3^+$ Tregs [% of $CD4^+$ T cells] visWAT 9.6 ± 0.9, $p < 0.01$; Figures 1D–1F).

Consistent with the increased Treg induction capacity, there was a lower proliferative potential in T cells from BAT and scWAT when compared with visWAT ($CD4^+Ki67^+$ T cells mean fluorescence intensity [MFI]: BAT 2,050 ± 50 versus scWAT $CD4^+Ki67^+$ T cells 3,025 ± 75 versus visWAT $CD4^+Ki67^+$ T cells 4,235 ± 45, $p < 0.01$; Figure 1G).

Cold Exposure Enhances Treg Induction of Adipose Tissue T Cells

Brown/beige fat thermogenesis is stimulated by environmental cold as a means to enhance sympathetic tone. To dissect if and how Tregs interlink thermal challenges with adipocyte function, we first investigated the effects of cold exposure. Cold acclimation (1 week at 8°C) significantly increased $Foxp3^+$ Treg percentages purified from inguinal lymph nodes (inLNs) of mice (Figures 1H and 1I). Short-term cold acclimation (24 hr at 4°C) likewise enhanced $Foxp3^+$ Treg percentages in T cells from BAT, scWAT, and visWAT ($CD4^+CD25^{++}Foxp3^+$ T cells [% of $CD4^+$ T cells]: BAT 7.4 ± 0.6 versus BAT after cold 11.6 ± 0.8, $p < 0.001$; scWAT 7.2 ± 0.2 versus scWAT after cold 15.9 ± 0.6, $p < 0.001$; visWAT 4.9 ± 0.3 versus visWAT after cold 8.8 ± 0.4, $p < 0.001$; Figure 1J).

In addition, Treg induction of naive $CD4^+$ T cells from the respective fat depots after 24 hr of cold was significantly enhanced (Figure 1K).

Short-Term Exposure to a High-Calorie Environment Increases $Foxp3^+$ Tregs in BAT

Short-term high-caloric diets promote BAT thermogenesis (Rothwell and Stock, 1979), which depends on uncoupling protein 1 (UCP1 function; Feldmann et al., 2009).

A 2-week high-fat/high-sugar (HFHS) diet environment to 6-week-old Bl6 Foxp3-GFP reporter mice or 8-week-old BALB/c Foxp3-GFP reporter mice significantly enhanced $Foxp3^+$ Treg accumulation in BAT (Figures 1L and 1M). Mild changes in Tregs were seen in scWAT, whereas the 2-week HFHS diet resulted in a significant decline in visWAT Treg percentages (Figures 1L and 1M). HFHS diet exposure for 8 weeks did not alter Treg ratios in BAT or scWAT of B6 Foxp3-GFP reporter mice. In accordance with earlier reports (Cipolletta et al., 2012, 2015) indicating local Treg expansion in visWAT in this age group (~14 weeks of age), we found higher Treg ratios on the standard diet. In contrast to higher Treg percentages residing in BAT and scWAT, Treg percentages in visWAT were severely reduced by HFHS diet exposure (Figure 1N). An HFHS diet for 16 weeks left $Foxp3^+$ Tregs in BAT unaltered and only mildly reduced them in scWAT of BALB/c mice, while percentages of $Foxp3^+$ Tregs in visWAT were significantly reduced by high-caloric challenge (Figure 1O).

In accordance with the increase of BAT-residing Tregs after 2 weeks on the HFHS diet, the Treg induction potential of naive $CD4^+$ T cells was likewise significantly enhanced (Figures S1A and S1B).

Beta-Adrenergic Stimulation Increases $Foxp3^+$ Treg Induction *In Vivo*

Given the results on cold exposure or a short-term high-calorie environment to enhance sympathetic tone and support BAT thermogenesis, we next directly increased sympathetic tone and assessed local Treg induction using ADRB3 agonists. Previous studies as well as *in silico* analyses (Heng et al., 2008) suggested *Adrb3* expression, which encodes for the ADRB3 in human and murine lymphocytes (Yu et al., 2007).

ADRB3 stimulation to young BALB/c Foxp3 GFP reporter mice *in vivo* (2 days, 1 mg/kg intraperitoneally [i.p.]) with the beta3 receptor agonist CL-316243 (CL) enhanced Foxp3 abundance in $CD4^+$ T cells from inLNs as well as from fat (Figures 2A–2D; negative staining controls in Figure S1C). Treg induction with naive $CD4^+$ T cells was most prominently increased in T cells from BAT and scWAT compared with visWAT (Figure 2E).

Treg Induction Is Impaired in the Absence of Beta-Adrenergic Receptors *In Vivo*

To mechanistically dissect the link among beta3-adrenergic signaling, Treg induction, and AT function, we next analyzed betaless mice, which lack all three beta-adrenergic receptors (Bachman et al., 2002). This loss-of-function model had significantly decreased Treg percentages in inLNs and scWAT depots (Figures 2F–2H). Likewise, Treg induction using naive $CD4^+$ T cells from fat depots of betaless mice was reduced when compared with wild-type (WT) animals (Figure 2I).

Treg Induction by Sympathetic Drive Is Required for Normal Adipose Tissue Function

To determine if and how Tregs interconnect an enhanced sympathetic tone with changes in AT function, we next performed loss-of-function experiments. Specifically, ADRB3 stimulation *in vivo* (CL for 3 days, 1 mg/kg, i.p.) induces genes relevant for BAT function (Figure S1D). In a first set of loss-of-function studies, Tregs were depleted in BALB/c Foxp3-GFP reporter mice prior to the start of ADRB3 stimulation by the use of established procedures involving anti-CD25 antibody application (Setiady et al., 2010) (Figures 3A and S1E). Treg-depleted mice (control stainings for Treg depletion efficacy in AT; Figure S1E) and control animals were injected with CL. In control mice without Treg depletion, canonical thermogenic gene programs (*Ucp1*, *Ppargc1a*, *Prdm16*, and *Cidea*) were induced in BAT following ADRB3 stimulation. In contrast, this induction by ADRB3 stimulation was blunted in mice with Treg depletion (Figure 3C). Accordingly, upon ADRB3 stimulation, we found surrogate markers of β-oxidation (*Acox1* and *Ascl1* gene expression) as well as lipolysis (*Lpl*, *Lipe* gene expression) to be upregulated in BAT, and again, this induction did not occur in mice with depleted Tregs (Figure 3C). Moreover, in contrast to control mice treated with ADRB3 stimuli *in vivo*, BAT tissue of Treg-depleted CL-treated mice had significantly increased *Il6* gene expression (Figure 3C). Analyses of BAT tissue revealed a significant decline of *Plin1*, *Cycs*, *P2rx5*, *Glut1*, and *Adipoq* gene expression in Treg-depleted CL-treated mice (Figure S1F),

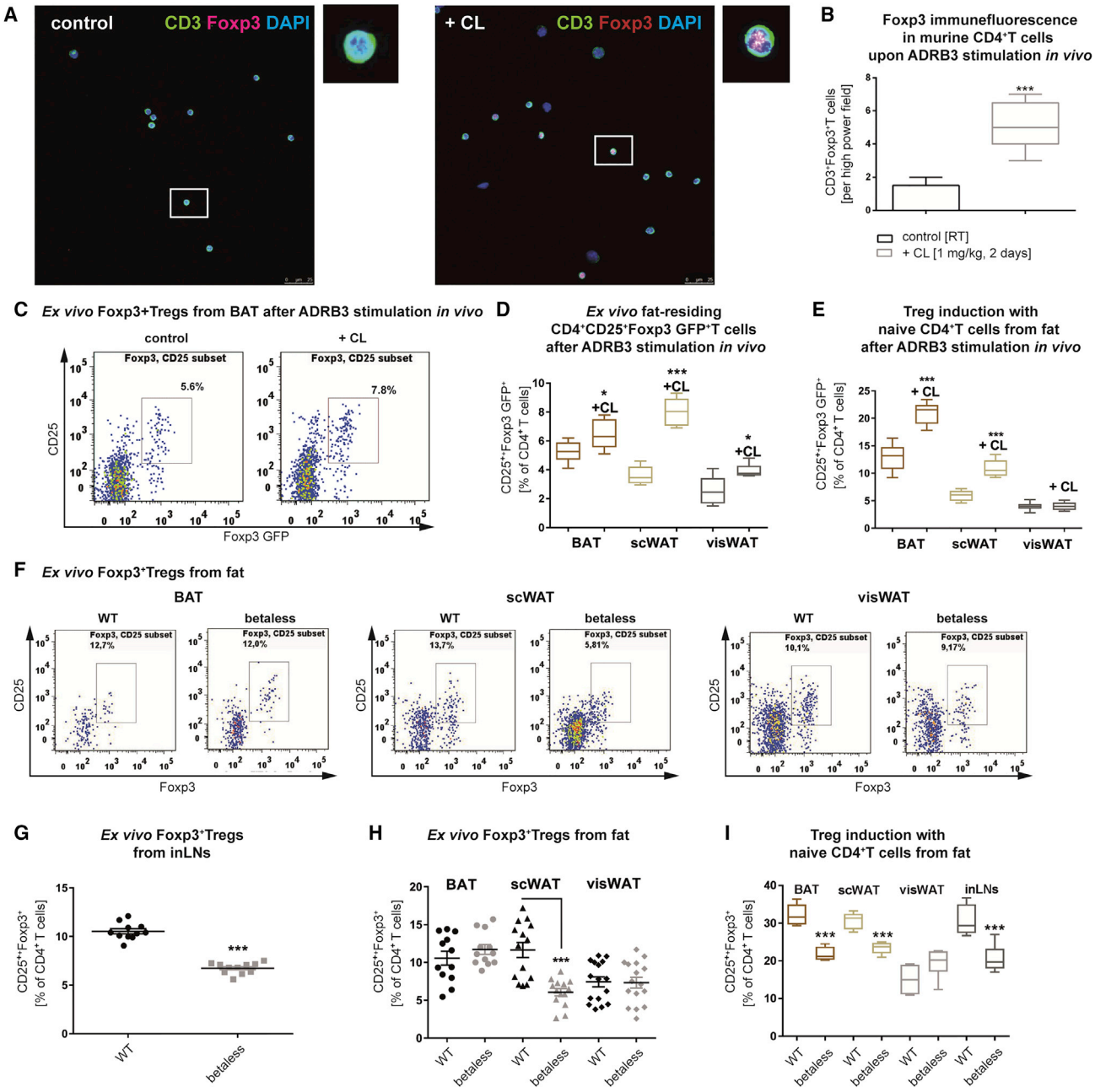

Figure 2. The Role of Beta-Adrenergic Signaling for Foxp3$^+$ Tregs

(A) Representative confocal microscopy images of CD4$^+$ T cells purified from BALB/c Foxp3GFP reporter mice after *in vivo* CL treatment (2 days, 1 mg/kg i.p.). Scale bar, 25 μm.

(B) Foxp3$^+$CD3$^+$ T cells per high power field in samples from (A). n = 5 per group, p = 0.0003.

(C) Representative FACS plots for the identification of *ex vivo* CD4$^+$CD25$^+$Foxp3GFP$^+$ Tregs from BAT upon *in vivo* CL treatment (3 days, 1 mg/kg i.p.). Plots are pre-gated as shown in Figure 1A.

(D) Summary graph for *ex vivo* Treg frequencies purified from AT of young BALB/c mice as in (C). n = 6 per group.

(E) Summary graph for *in vitro* Treg induction assays with naive CD4$^+$ T cells from ATs after *in vivo* treatment with CL (3 days, 1 mg/kg i.p.). n = 6 per group.

(F) Representative FACS plots for the identification of *ex vivo* CD4$^+$CD25^{++}Foxp3$^+$ Tregs from fat depots of WT or betaless mice.

(G and H) Summary graph for *ex vivo* Treg frequencies purified from inLNs (G; n = 11) or fat depots (H; n > 12 per group) of WT or beta-less mice. n = 11 per group.

(I) Summary graph for *in vitro* Treg induction assays of naive CD4$^+$ T cells purified from fat depots or inLNs of WT or betaless mice. n = 6 per group.

See also Figure S1. Data are presented as box-and-whisker plots with min and max values for data distribution or as mean ± SEM. *p < 0.05, ***p < 0.001.

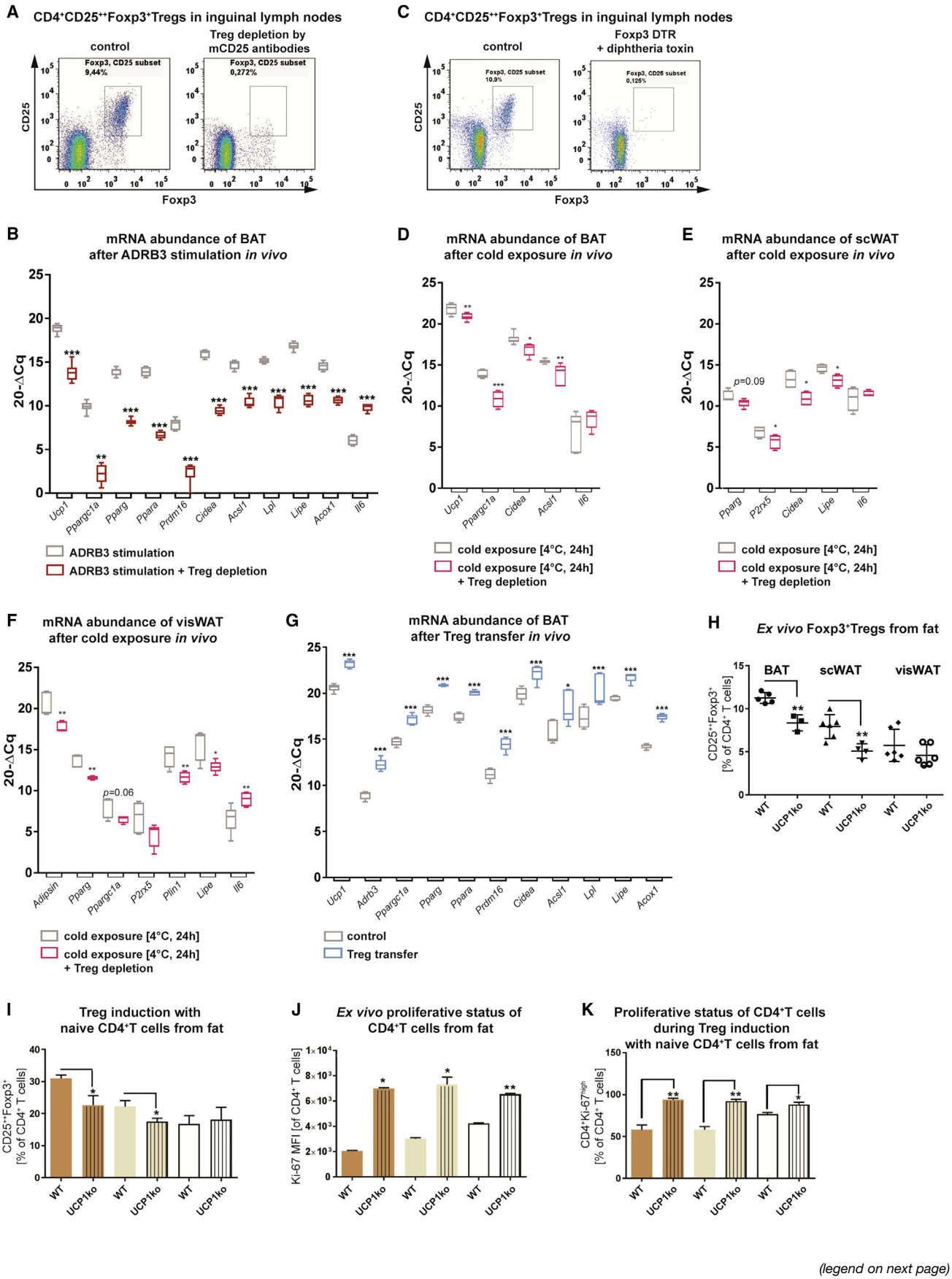

(legend on next page)

thereby revealing a role of Foxp3$^+$ Tregs in regulating lipolysis and thermogenesis in BAT.

To further dissect the mutual crosstalk between Tregs and AT during diet-induced thermogenesis, Tregs were likewise depleted prior to exposure to a 1-week HFHS diet challenge. Such loss of function by anti-CD25 antibodies significantly reduced thermogenic BAT gene programs including *Ucp1*, *Ppargc1a*, *Pparg*, *Ppara*, and *Prdm16* (Figure S2A). In addition, β-oxidation- (*Ascl1*) as well as lipolysis-related genes (*Lipe*) were reduced in Treg-depleted mice. Furthermore, expression of *Cycs*, *P2rx5*, and *Adipsin* was also decreased in BAT of Treg-depleted mice (Figure S2A). The responses in scWAT were more heterogeneous; Treg depletion promoted a significant decline in *Pparg*, *Prdm16*, and *Acsl1* (Figure S2B).

In a second set of loss-of-function studies, we used C57BL/6 Foxp3-DTR mice (Kim et al., 2007) and diphtheria toxin (DT)-mediated Treg depletion to confirm the results seen in Treg-depleted animals using anti-CD25 antibodies. Accordingly, upon ADRB3 stimulation, Treg-depleted Foxp3-DTR mice (Figures 3C and 3D) exposed to cold (4°C for 24 hr) had a significant reduction in thermogenic gene expression, including *Ucp1*, *Ppargc1a*, and *Cidea* and in β-oxidation genes such as *Acsl1* in BAT, while *Il6* levels mildly increased (Figure 3D; control stainings for Treg depletion in fat; Figure S2C). Treg loss of function mildly reduced scWAT function as indicated by a decline in *Pparg*, *P2rx5*, *Cidea*, and *Lipe* expression (Figure 3E). Moreover, upon DT-mediated Treg depletion and cold exposure, we found expression levels of *Adipsin*, *Pparg*, *Ppargc1a*, *P2rx5*, *Plin1*, and *Lipe* to be decreased in visWAT, while *Il6* were significantly upregulated (Figure 3F).

Foxp3$^+$ Tregs Control Adipose Tissue Function

To directly assess the role of Foxp3$^+$ Tregs in regulating AT function, we performed gain-of-function experiments by *in vivo* transfers of CD25$^+$Foxp3GFP$^+$ Tregs into respective BALB/c recipient mice (intravenous or intraperitoneal transfer). Analyses of BAT function 1 week after transfer revealed a significant enhancement of thermogenic genes (*Ucp1*, *Adrb3*, *Ppargc1a*, *Prdm16*, and *Cidea*) in BAT (Figure 3G). Consistent with this, there were increased levels of mRNA of β-oxidation-related genes (*Acox1* and *Ascl1*) as well as of lipolysis-related genes (*Lpl* and *Lipe*) in BAT after the Treg transfer (Figure 3G). In addition, *Plin1*, *Cycs*, *P2rx5*, *Glut1*, and *Adipoq* were all enhanced in BAT after Treg transfer (Figure S3A). Mild changes were also seen after Treg transfer in scWAT, with *Ppara*, *Prdm16*, *Cpt1b*, and *Glut1* being upregulated (Figure S3B). The Treg-mediated improvement of BAT function (thermogenic capacity and lipolytic function) upon Treg transfer (Figure 3G) was equal, or partially superior to, that which occurred with ADRB3 agonist treatment *in vivo*.

We next employed *in situ* expansion of Foxp3$^+$ Treg cells using subcutaneous injections of interleukin (IL)-2/mAb complexes (3 days, 6 μg/day) as a second gain-of-function model. These complexes cause a selective expansion of Foxp3$^+$ Tregs (Daniel et al., 2010; Webster et al., 2009). Following Foxp3$^+$ Treg expansion, there was a significant enhancement of thermogenic genes (*Ucp1*, *Ppargc1a*, *Prdm16*, and *Cidea*) in scWAT, accompanied by increased levels of β-oxidation- (*Acox1* and *Acsl1*) and lipolysis-related genes (e.g., *Lipe* and *Plin1*; Figures S3C and S3D) and increased *P2rx5*, *Pparg*, *Ppara*, and *Adipsin* expression.

Gain of function by Treg expansion also had a mild impact on visWAT metabolic function. Specifically, genes related to differentiation (*Pparg*), adipogenesis (*Adipsin*), browning (*Cd137*), and lipolysis (*Acox1*, *Lipe*, *Lpl*, and *Plin1*) (Figure S3E) were all upregulated.

Treg Induction in BAT Is Impaired in the Absence of UCP1

To determine whether Treg-adipose crosstalk in BAT also includes a functional programming of BAT-residing T cells, we next investigated a BAT loss-of-function model. Specifically, the thermogenic activity of brown fat cells relies, to a great extent, on UCP1, which is localized on the inner membrane of BAT mitochondria. Upon activation, UCP1 catalyzes the leak of protons across the mitochondrial membrane (Fedorenko et al., 2012), uncoupling oxidative respiration from ATP synthesis, while the resulting energy derived from substrate oxidation is dissipated as heat.

Therefore, we used UCP1-ablated (UCP1ko) mice to dissect whether the fat thermogenic response causes Treg activation or whether Treg activity is required for thermogenic responses. The percentages of locally residing CD4$^+$CD25^{++}Foxp3$^+$ Tregs purified from fat depots of young UCP1ko mice were reduced in BAT and scWAT, whereas marginal or no changes occurred in visWAT (Figures 3H and S4A). Likewise, Treg induction was lower in naive CD4$^+$CD25$^-$ T cells purified from BAT and scWAT of UCP1ko mice when compared with WT T cells (Figures 3I

Figure 3. Foxp3$^+$ Tregs Regulate Adipose Tissue Function and Vice Versa

(A and C) Representative FACS plots demonstrating Treg depletion efficacy in inLNs after (A) 3 days of mCD25 antibody treatment of WT mice or (C) 48 hr after diphtheria toxin administration to Foxp3 DTR mice.

(B) mRNA expression of genes involved in BAT function upon treatment with CL *in vivo* in the presence or absence of Tregs. Tregs were depleted using anti-CD25 antibodies. n = 6 per group.

(D–F) mRNA expression of genes involved in BAT (D), scWAT (E), and visWAT (F) function after cold exposure (4°C, 24 hr) in the presence or absence of Tregs. Tregs were depleted in Foxp3 DTR mice by administration of DT. n = 6 per group.

(G) In gain-of-function experiments, CD4$^+$CD25$^+$Foxp3GFP$^+$ Tregs were adoptively transferred into congenic recipients. Analyses of BAT function by qPCR were performed 1 week after transfer. n = 6 per group.

(H) Summary graph for *ex vivo* Treg frequencies purified from BAT, scWAT, and visWAT of WT or UCP1ko animals. n = 5–6 for WT mice and n = 4–6 for UCP1ko animals.

(I) Summary graph for *in vitro* Treg induction assays of naive CD4$^+$ T cells purified from fat depots of WT or UCP1ko animals. n = 5 per group.

(J) Summary graph for the *ex vivo* proliferative status of CD4$^+$ T cells from fat depots of WT and UCP1ko mice as assessed by analysis of Ki67 mean fluorescence intensity (MFI). n = 5 per group.

(K) Shown is the proliferative status of CD4$^+$ T cells during Treg induction assays from fat depots of WT and UCP1ko mice as assessed by analysis of Ki67^{high}.

See also Figures S1–S4. Data are presented as box-and-whisker plots with min and max values for data distribution. *p < 0.05, **p < 0.01, ***p < 0.001.

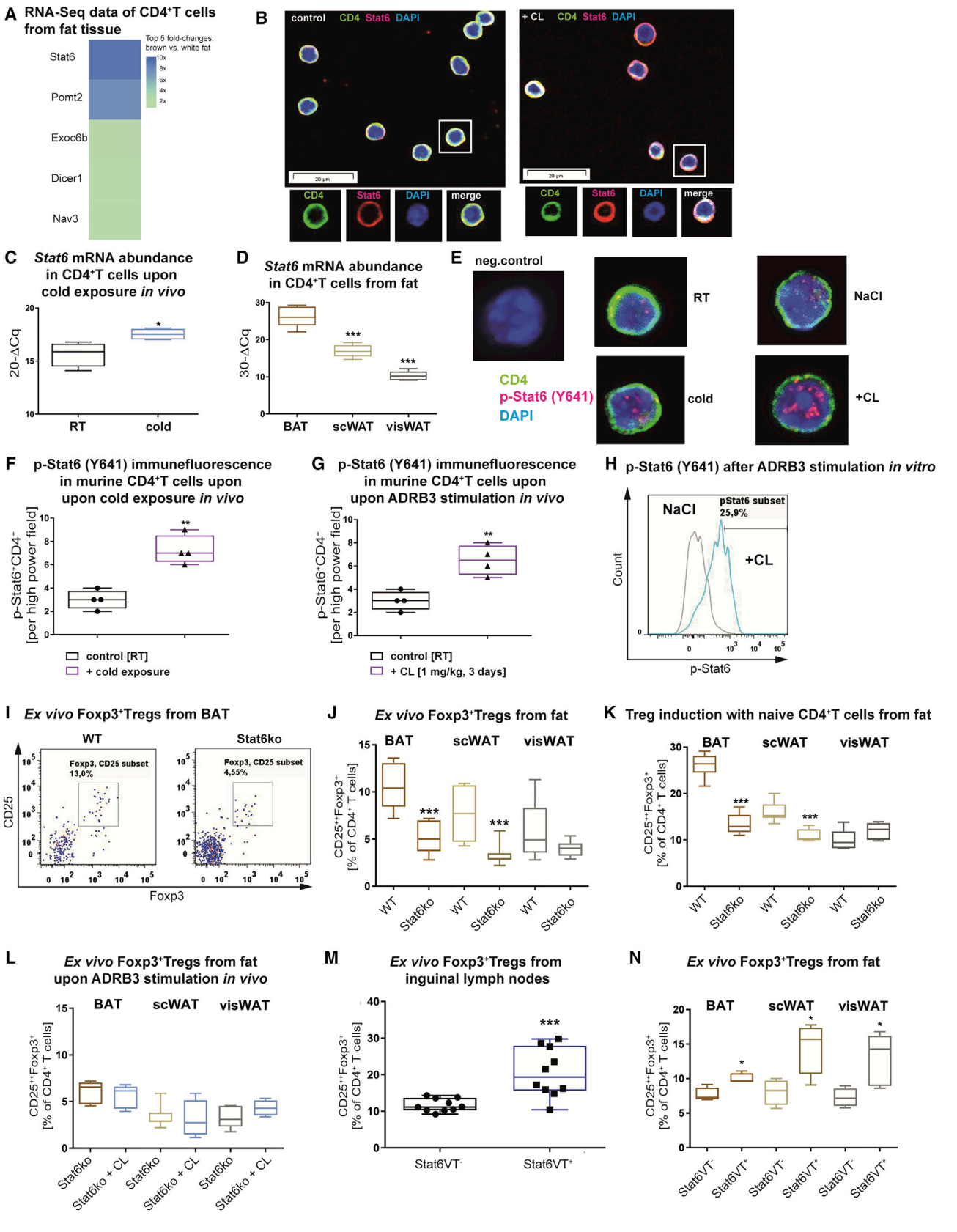

(legend on next page)

and S4B). The reduced Treg percentages and their lower Treg induction potential were accompanied by a higher proliferative potential in local $CD4^+CD25^-$ T cells from UCP1ko mice when compared with littermate controls, both *ex vivo* and upon TCR stimulation *in vitro* (Figures 3J, 3K, and S4C). These data imply the existence of a mutual crosstalk between Treg cells and AT in that the local tissue environment affects T cell differentiation and function, which in turn can influence tissue function and organismal homeostasis.

$CD4^+$ T Cells from BAT Show Higher *Stat6* Abundance than WAT

We next aimed to identify molecular underpinnings of the functional interplay between Treg cells and AT that are linked with cold exposure and beta3-adrenergic stimulation in scWAT and BAT. When comparing the gene expression patterns of murine $CD4^+$ T cells from young BALB/c Foxp3-GFP reporter mice at room temperature (RT) in a pilot experiment, we observed higher levels of transcripts encoding the transcription factor *Stat6* in BAT compared to WAT (Figure 4A).

In vivo application of an ADRB3 agonist (2 days CL, 1 mg/kg i.p.) resulted in increased *Stat6* expression in $CD4^+$ T cells (Figure 4B; see quantification in Figure S5A). Moreover, *in vivo* cold exposure (1 week, 8°C) induced *Stat6* mRNA expression in $CD4^+$ T cells (Figure 4C). When *Stat6* expression levels in fat-residing $CD4^+$ T cells of BALB/c Foxp3-GFP reporter mice were verified, there was higher *Stat6* expression in $CD4^+$ T cells from BAT than in scWAT or visWAT (Figure 4D).

Short-term cold exposure (4°C, 24 hr) and ADRB3 stimulation (3 days CL, 1 mg/kg i.p.) likewise induced phosphorylation of Stat6 at position pY641 in $CD4^+$ T cells (Figures 4E–4G). Moreover, the percentage of cells that are p-Stat6 positive (and the MFI of the entire population) was increased in pre-activated $CD4^+$ T cells after ADRB3 stimulation for 15 min *in vitro* (100 nM CL; Figure 4H).

Stat6 has been implicated in promoting cold-induced remodeling of fat. For instance, cold-induced expression of *Ucp1* in scWAT was reported to be severely decreased in *Stat6*$^{-/-}$ (Stat6ko) mice (Qiu et al., 2014). From an immunological perspective, Stat6 promotes Th2 and Th9 immunity (Goenka and Kaplan, 2011). However, recent studies pointed to a positive role for Stat6 as a second required signal in antigen-specific Treg induction (Chapoval et al., 2010; Pillemer et al., 2009; Sanchez-Guajardo et al., 2007), while in Stat6VT transgenic mice, the constitutive activation of Stat6 in $CD4^+$ T cells increased the percentages of peripheral Tregs (Sanchez-Guajardo et al., 2007).

Treg Induction in Adipose Tissue Requires Stat6

Local Treg ratios [$CD4^+CD25^{++}Foxp3^+$ T cells [% of $CD4^+$ T cells] BAT, WT 10.5 ± 0.7 versus Stat6ko 5.2 ± 0.5, $p < 0.001$; scWAT, WT 7.7 ± 0.9 versus Stat6ko 3.2 ± 0.3, $p = 0.0003$; Figures 4I and 4J) and Treg induction of naive T cells purified from fat depots of BALB/c Stat6ko (Gessner et al., 2005; Kaplan et al., 1996) were significantly blunted in the absence of Stat6 ($CD4^+CD25^+Foxp3^+$ T cells [% of $CD4^+$ T cells] BAT, WT 26.1 ± 1.0 versus Stat6ko 13.4 ± 0.9, $p < 0.001$; scWAT, WT 16.0 ± 0.9 versus Stat6ko 10.8 ± 0.5, $p < 0.001$; Figure 4K). In a second approach, a pharmacological Stat6 inhibitor significantly reduced Treg induction using naive $CD4^+$ T cells from inguinal lymph nodes of BALB/c Foxp3-GFP reporter mice (Figure S5B). ADRB3 stimulation/blockade *in vitro* (Figures S5C and S5D) or *in vivo* (CL 1 mg/kg, i.p., 3 days; Figure 4L) did not affect Treg induction in the absence of Stat6.

Since T cell-specific Stat6ko mice are not available for loss-of-function studies, we used *in vivo* T cell transfer experiments to assess T cell-intrinsic effects of Stat6 relevant for Treg induction upon beta3-adrenergic stimulation. We purified naive $CD4^+$ T cells from WT and Stat6ko animals and transferred them into congenic CD90.1 BALB/c hosts to permit re-identification of transferred cells. In addition, mice were treated for 3 days with CL at 1 mg/kg, i.p., *in vivo*. Re-analysis of transferred cells revealed that in accordance with previous studies, Treg induction capacities *in vivo* in polyclonal TCR repertoires were low, although we found the percentages of induced Tregs to be significantly reduced in T cells transferred from Stat6ko mice

Figure 4. Stat6 Regulates Treg Accumulation in Adipose Tissue

(A) Depicted are the top five fold changes for upregulated genes in $CD4^+$ T cells purified from brown versus white fat by mRNA expression profiling. The cutoff for reading counts was set to 30 and pseudogenes have been manually removed.

(B) Representative confocal microscopy images of $CD4^+$ T cells purified from BALB/c control mice or BALB/c mice after *in vivo* treatment with CL (3 days, 1 mg/kg i.p.). Scale bar, 20 μm.

(C) qRT-PCR analyses of *Stat6* mRNA abundance in $CD4^+$ T cells purified from BALB/c mice upon cold exposure (1 week, 8°C). n = 4 mice per group from two independent experiments.

(D) *Stat6* mRNA expression in $CD4^+$ T cells purified from BAT, scWAT, or visWAT of young lean BALB/c mice. n = 5 mice per group.

(E) Representative confocal microscopy images for p-Stat6 induction in $CD4^+$ T cells from inLNs after CL treatment (3 days at 1 mg/kg i.p.) and *in vivo* cold exposure (24 hr, 4°C).

(F) Quantification of p-$Stat6^+CD4^+$ T cells per high power field in samples from (E) after cold exposure. n = 4 per group.

(G) Quantification of p-$Stat6^+CD4^+$ T cells per high power field in samples from (E) after CL treatment. n = 4 per group.

(H) Histogram of p-Stat6 detection in pre-activated $CD4^+$ T cells after 10 nM CL stimulation for 15 min *in vitro*.

(I) Representative FACS plots for the identification of *ex vivo* $CD4^+CD25^{++}Foxp3^+$ Tregs from BAT of WT or Stat6ko mice.

(J) Summary graph for *ex vivo* Treg frequencies purified from fat depots of WT mice or Stat6ko mice. n = 10 per group.

(K) Summary graph for *in vitro* Treg induction assays of naive $CD4^+$ T cells purified from fat depots of WT or Stat6ko mice. n = 6 per group.

(L) Summary graph for *in vitro* Treg induction assays of naive $CD4^+$ T cells purified from BAT, scWAT, and visWAT Stat6ko mice that were treated with vehicle or CL (3 days, 1 mg/kg) *in vivo*.

(M) Representative FACS blots for *ex vivo* Treg frequencies purified from inLNs of WT mice or mice with constitutively active Stat6 (Stat6VT mice). n = 10 per group.

(N) Summary graph for *ex vivo* $CD4^+CD25^{++}Foxp3^+$ Treg frequencies purified from fat depots of $Stat6VT^+$ or $Stat6VT^-$ mice. n = 4 per group.

See also Figure S5. Data are presented as box-and-whisker plots with min and max values for data distribution. *$p < 0.05$, **$p < 0.01$, ***$p < 0.001$.

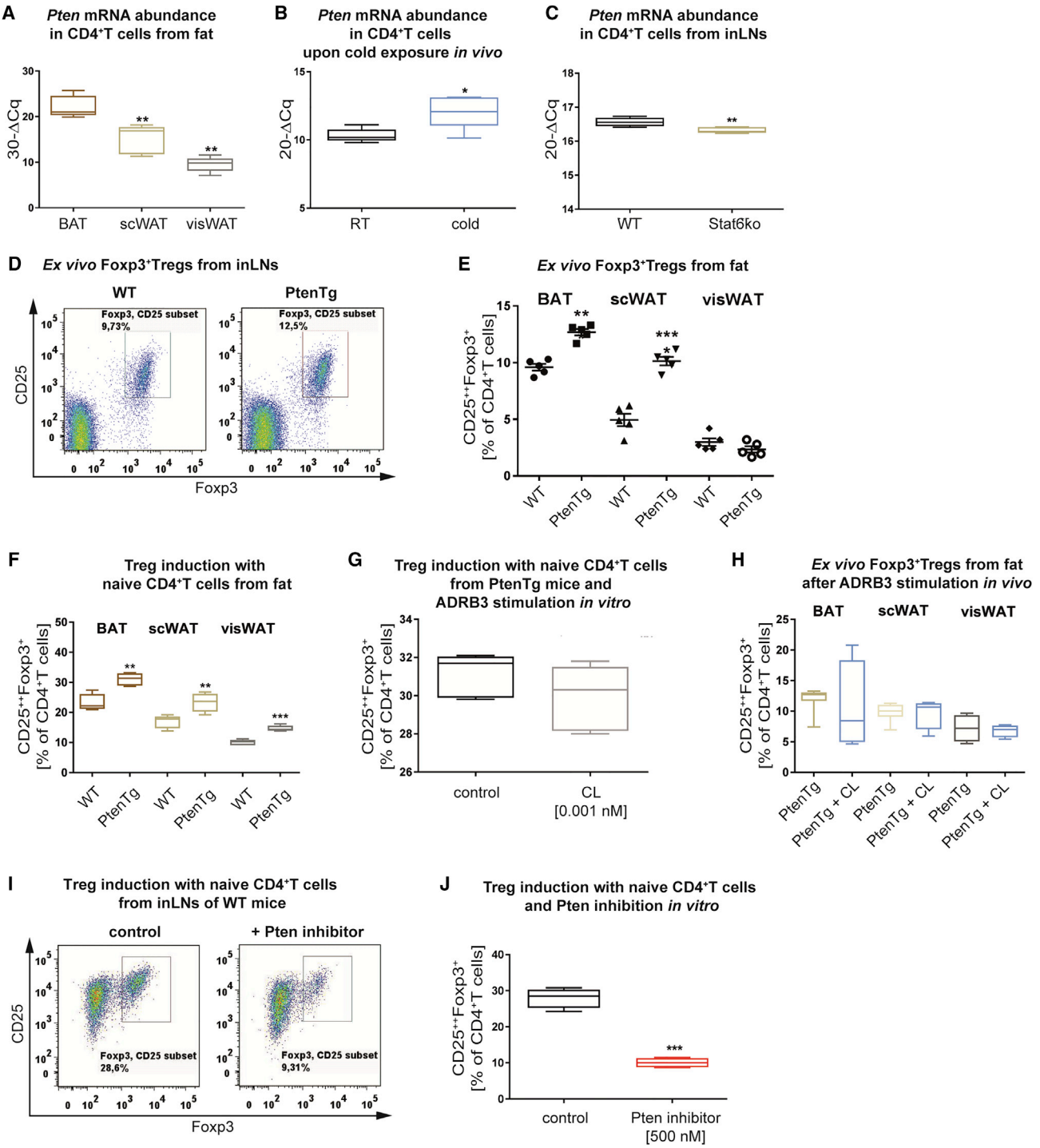

Figure 5. Role of Pten in Treg Accumulation of Fat-Residing CD4+ T Cells

(A–C) qRT-PCR analyses of *Pten* mRNA abundance in CD4+ T cells purified from (A) BAT, scWAT, or visWAT of young lean BALB/c animals (n = 5 per group), (B) inLNs after *in vivo* cold exposure of BALB/c animals (n = 5 per group), and (C) in CD4+ T cells purified from inLNs of Stat6ko animals (n = 4 per group).

(D) Representative FACS plots identifying *ex vivo* CD4+CD25++Foxp3+ Tregs from inLNs of WT or mice transgenetically overexpressing *Pten* (PtenTg animals).

(E) Summary graph for the identification of *ex vivo* CD4+CD25++Foxp3+ Tregs purified from BAT, scWAT, or visWAT of WT or PtenTg mice. n = 5 per group.

(F) Summary graph for *in vitro* Treg induction assays using limited TCR stimulation of naive CD4+ T cells purified from fat depots of WT or PtenTg animals. n = 6 per group.

(G) Summary graph for *in vitro* Treg induction assays using limited TCR stimulation of naive CD4+ T cells of PtenTg animals in the presence or absence of ADRB3 stimulation (0.001 nM CL). n = 5 per group.

(legend continued on next page)

($CD4^+CD25^{++}Foxp3^+$ T cells [% of $CD4^+$ T cells]: WT 3.8 ± 0.9 versus Stat6ko 1.5 ± 0.3, p = 0.0200; Figure S5E).

Treg-Adipose Crosstalk Induced by ADRB3 Stimulation Requires Stat6 *In Vivo*

To determine whether the impaired Treg induction in fat depots of Stat6ko mice is associated with altered AT function, we examined AT function of Stat6ko mice upon ADRB3 stimulation *in vivo*. In contrast to WT mice (Figure S5F), ADRB3 stimulation of Stat6ko mice *in vivo* did not increase genes important for BAT function (no upregulation was seen for *Ucp1*, *Ppargc1a*, *Cidea*, *Ascl1*, *Plin1*, *Lipe*, or *P2rx5*), while ADRB3 stimulation in the absence of Stat6 significantly reduced *Pparg* abundance (p = 0.0117) and *Adipsin* (p = 0.0388) (Figure S5F). Genes related to thermogenesis, lipolysis, and adipose differentiation were likewise unaffected by ADRB3 stimulation in scWAT from Stat6ko animals, while ADRB3 stimulation significantly reduced *Ucp1*, *Pparg*, *Lipe*, *Adipsin*, and *P2rx5* in visWAT of Stat6ko mice (Figures S5G and S5H).

Treg Induction Is Enhanced by a Constitutively Active Stat6

To address the relevance of Stat6 in mediating a functional interplay of Tregs and AT in gain-of-function experiments, we used mice with a constitutively active Stat6 expression in lymphoid cells (Bruns et al., 2003; Sehra et al., 2008) ($Stat6VT^+$ versus $Stat6VT^-$ littermates). We identified increased $Foxp3^+$ Treg frequencies in inLNs ($CD4^+CD25^{++}Foxp3^+$ T cells [% of $CD4^+$ T cells]: $Stat6VT^-$ 11.7 ± 0.5 versus $Stat6VT^+$ 20.6 ± 2.1, p = 0.0007; Figure 4M). *Ex vivo* Treg frequencies from AT of $Stat6VT^+$ mice had higher variability but were increased when compared with $Stat6VT^-$ littermates (Figure 4N). In the steady state, without ADRB3 stimulation or cold exposure, $Stat6VT^+$ mice had increased *Pparg*, *Adipsin*, and *P2rx5* abundance in fat (Figures S5I–S5K).

Treg Induction in BAT Is Driven by Pten Signaling

Phosphatase and tensin homolog (Pten) has been implicated in positively regulating BAT tissue function; e.g., by promoting *Ucp1* expression (Ortega-Molina et al., 2012). We therefore studied Pten as a second potential signaling intermediate linking the interplay between Tregs and AT function given the impaired Treg induction in UCP1ko animals. Animals with overexpression of *Pten* presented with a hyperactive BAT and harbored increased *Ucp1* levels in BAT (Ortega-Molina et al., 2012). Pten also regulates Treg induction (Sauer et al., 2008; Shrestha et al., 2015). We observed increased *Pten* expression in $CD4^+$ T cells from BAT and scWAT of BALB/c mice (Figure 5A). In accordance with the results for *Stat6* expression, *in vivo* cold exposure significantly increased *Pten* expression in $CD4^+$ T cells (Figure 5B). In $CD4^+$ T cells from inLNs of Stat6ko mice, *Pten* expression levels were mildly diminished when compared with WT animals (Figure 5C). For a gain-of-function approach, we used *Pten*-overexpressing mice (PtenTg) and found them to have significantly increased $Foxp3^+$ Treg percentages in inLNs, BAT, and scWAT when compared with WT animals ($CD4^+CD25^{++}Foxp3^+$ T cells [% of $CD4^+$ T cells] BAT, WT 9.6 ± 0.2 versus PtenTg 12.7 ± 0.2, p < 0.001; scWAT, WT 4.9 ± 0.5 versus PtenTg 10.1 ± 0.3, p < 0.001; Figures 5D and 5E). In addition, Treg induction was significantly enhanced in naive $CD4^+$ T cells of PtenTg animals (Figure 5F). Levels of *Pten* overexpression varied in $CD4^+$ T cells from PtenTg animals (~4- to ~40-fold). Mice with higher levels of *Pten* overexpression (~40-fold over WT) harbored significantly more $Foxp3^+$ Tregs in all ATs, including visWAT (Figure S5L). No further increase in Treg induction was observed *in vitro* upon ADRB3 stimulation using naive $CD4^+$ T cells from PtenTg animals (Figure 5G). In addition, ADRB3 stimulation *in vivo* did not alter Treg percentages in AT of PtenTg mice (Figure 5H). A Pten inhibitor significantly reduced Treg induction *in vitro* using naive $CD4^+$ T cells from WT mice (Figures 5I and 5J).

Cold Exposure or ADRB3 Stimulation Induces a Treg-Inducing Proteome Signature

For an unbiased approach, we performed quantitative mass spectrometry-based proteomics (Meissner and Mann, 2014) to evaluate proteome compositions in $CD4^+$ T cells upon *in vivo* cold acclimation of mice (1 week, 8°C) or treatment with an ADRB3 agonist (3 days CL, 1 mg/kg, i.p.). We identified 5,031 proteins in sorted $CD4^+$ T cell proteomes of mice that were either exposed to cold or treated with CL *in vivo*, compared with control animals housed at room temperature (RT) or treated with NaCl, respectively. To verify Treg induction upon cold exposure or ADRB3 stimulation *in vivo* at the protein level, we focused on proteins associated with selected Gene Ontology terms Biological Function (GOBP) related to negative regulation of immune responses/effector responses, as well as Treg induction and Foxp3 regulatory networks. Unsupervised hierarchical clustering conditions revealed upregulation of several GO terms related to Treg induction, among them Stat6 and Foxp3 (Figures 6A and 6B). Similarly, several proteins of the Foxp3 regulatory network were found to be mildly upregulated upon cold exposure or ADRB3 stimulation (Figures 6C and 6D).

Next, to integrate the relevance of Stat6 for linking ADRB3 stimulation with Treg induction in an unbiased setting, we examined proteome compositions in $CD4^+$ T cells from Stat6ko mice with or without ADRB3 stimulation *in vivo*. We identified 2,827 proteins in sorted $CD4^+$ T cell proteomes of Stat6ko mice that were treated with CL *in vivo*, compared with control mice given NaCl, respectively. Unsupervised hierarchical clustering revealed that in the absence of Stat6 upon ADRB3 stimulation *in vivo*, several GO terms related to Treg induction were downregulated, among them Foxp3 (Figure 6G). Overall, these data

(H) *Ex vivo* Treg frequencies purified from fat depots of PtenTg mice upon *in vivo* ADRB3 stimulation (3 days, 1 mg/kg CL). n = 8 for PtenTg control group and n = 4 for PtenTg + CL group.

(I) Representative FACS plots for *in vitro* Treg induction assays with or without Pten inhibitor (500 nM) using naive $CD4^+$ T cells purified from inLNs of WT mice.

(J) Summary graph of Pten inhibition for *in vitro* Treg induction assays of naive $CD4^+$ T cells purified from inLNs of WT animals. n = 4 per group from two independent experiments.

See also Figure S5. Data are presented as box-and-whisker plots with min and max values for data distribution or as mean ± SEM. *p < 0.05, **p < 0.01, ***p < 0.001.

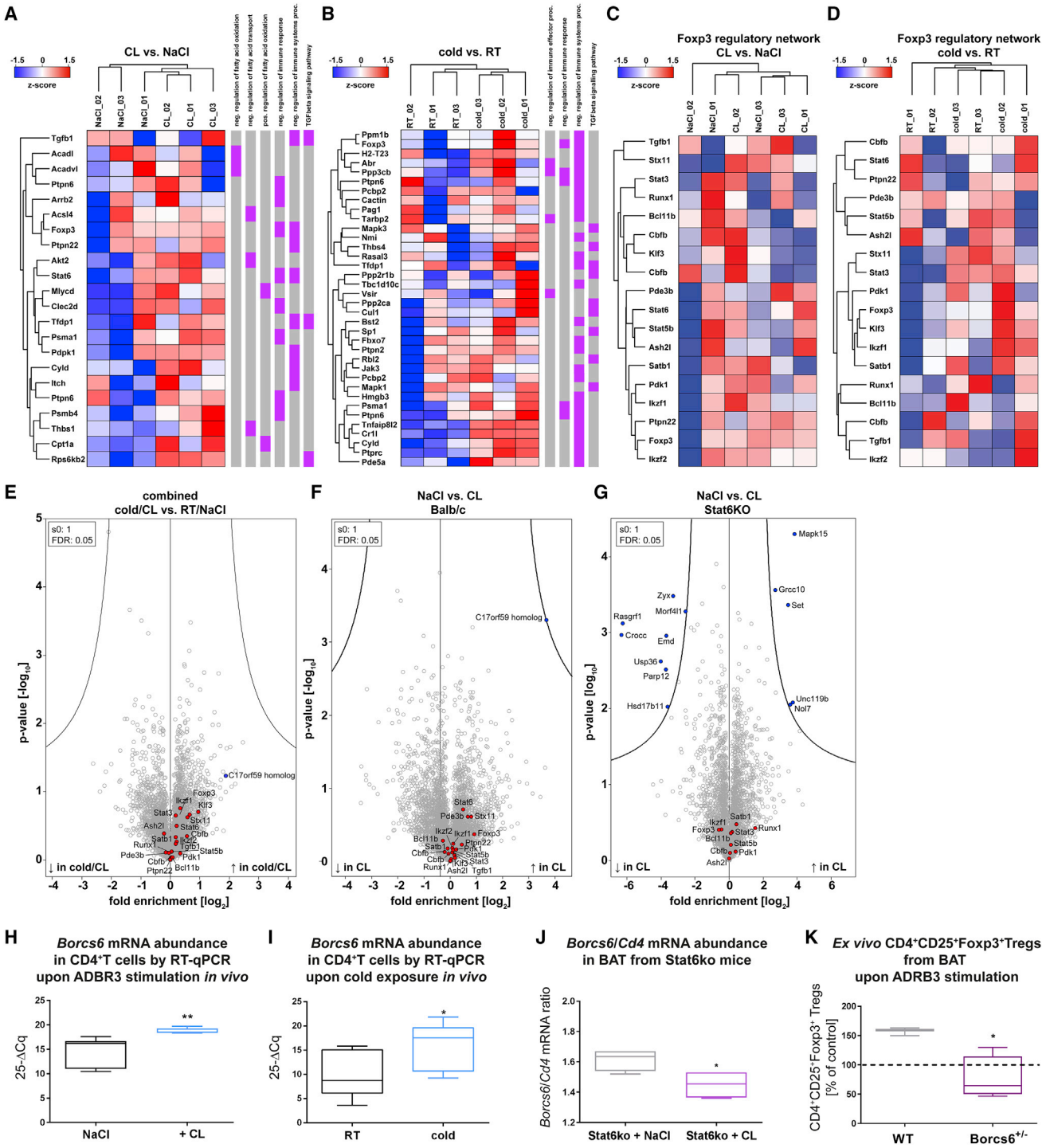

Figure 6. Cold Exposure or ADRB3 Stimulation Induces a Treg-Proneproteome Signature

(A and B) Proteins associated with selected Gene Ontology terms Biological Function (GOBP) were grouped using unsupervised hierarchical clustering of the *Z* scored MaxLFQ-intensities across the indicated experimental groups; CL versus NaCl (A) and cold versus RT (B). GOBP annotations are depicted in purple. (C and D) Proteins associated with the Foxp3 regulatory network were grouped as in (A) and (B) with groups: CL versus NaCl (C) and cold versus RT (D). (E–G) Combined volcano plot of the pairwise comparison between $CD4^+$ T cell proteomes purified from cold/CL- versus RT/NaCl-treated mice (E), NaCl- versus CL-treated mice (F) and NaCl- versus CL-treated Stat6ko mice (G). Expression fold changes (t test difference, log_2) were calculated and plotted against the t test p value ($-log_{10}$). Proteins associated with Foxp3 regulatory networks (red) and the C17orf59 homolog (blue) are highlighted. Their position on the right side of the plot indicates a higher abundance upon cold/CL (E) or CL treatment (F and G).

(legend continued on next page)

highlight that in Stat6-competent animals, either cold exposure or ADRB3 stimulation *in vivo* supports a tolerogenic proteome signature in $CD4^+$ T cells in accordance with identified increased Treg percentages and the induction of Foxp3 regulatory networks (Figures 6A–6D).

Importantly, $CD4^+$ T cells purified from mice subjected to cold exposure or else treated with CL *in vivo* had upregulated proteins involved in enhancing fatty acid oxidation (FAO), including Acsl4 and Cpt1a, as well as downregulation of proteins involved in negatively regulating FAO, including Acadvl and Acadl (Figures 6A, 6B, and 6E), thereby further supporting Treg induction and function (Chang and Pearce, 2016; MacIver et al., 2013).

Treg Induction in Adipose Tissue by Cold Exposure or ADRB3 Stimulation Involves C17orf59/Borcs6

Next, we combined both the cold/RT and the CL/NaCl datasets and performed pairwise comparison of the $CD4^+$ T cells. Besides the mild upregulation of the Foxp3 regulatory network, we identified C17orf59 as one of the most prominently upregulated proteins in $CD4^+$ T cells (Figure 6E for combined datasets; Figure 6F for CL treatment only). C17orf59 was reported to function as a Ragulator-interacting protein that inhibits mTORC1 activity through its interaction with Ragulator at the lysosome (Schweitzer et al., 2015). In accordance with previous studies (Daniel and von Boehmer, 2011; Sauer et al., 2008), inhibition of mTORC1 can directly enhance $Foxp3^+$ Treg induction (Daniel et al., 2010). C17orf59 was recently assigned a gene name, *BLOC-1-related complex subunit 6 (Borcs6)*. *Borcs6* mRNA levels were significantly increased in $CD4^+$ T cells from mice stimulated with ADRB3 (Figure 6F), and *Borcs6* mRNA levels were enhanced following ADRB3 stimulation and cold exposure *in vivo* (Figures 6H and 6I). We next aimed to link the increased *Borcs6* mRNA expression caused by ADRB3 stimulation with the observed mechanistic role of Stat6 for adjusting Treg induction and BAT function. In the absence of Stat6 ADRB3 stimulation, BAT of Stat6ko mice in fact had lowered *Borcs6*/*Cd4* mRNA ratios (Figure 6J).

In $Borcs6^{+/-}$ mice, the induction of $Foxp3^+$ Tregs in BAT following ADRB3 stimulation was significantly reduced when compared with WT mice (Figure 6K).

To validate the results by mass spectrometry, we first used immunofluorescence for C17orf59 in $CD4^+$ T cells together with confocal microscopy. C17orf59 protein expression was upregulated following cold exposure or ADRB3 stimulation *in vivo* (Figures 7A–7D). We also employed stimulated emission depletion (STED) microscopy for creating super-resolution images to analyze C17orf59 expression changes in cytoplasm of $CD4^+$ T cells purified from inguinal lymph nodes of mice upon cold exposure in further detail (Figure 7E). C17orf59 expression was enhanced in $CD4^+$ T cells from mice exposed to cold (24 hr, 4°C) when compared with animals at RT (Figure 7E). In line with the increased protein abundance of C17orf59 upon ADRB3 stimulation or cold exposure *in vivo*, we determined the intracellular localization of mTOR in $CD4^+$ T cells (Figures 7F–7H). While mTOR localizes more prominently to lysosomes in control $CD4^+$ T cells, it remained more diffuse in T cells from mice that had received ADRB3 stimulation *in vivo* or were exposed to cold (Figures 7F–7H). Both ADRB3 stimulation and cold exposure resulted in significantly reduced numbers of $mTOR^+Lamp2^+CD4^+$ T cells (Figures 7I and 7J). Finally, to integrate the findings on the role of Stat6 for Treg induction and AT function, we provide the first evidence that in the absence of Stat6, C17orf59 expression was reduced in the steady state when compared with WT mice (Figures 7K–7M). Consistent with this observation, $CD4^+$ T cells from $Stat6VT^+$ animals, which harbor a constitutively active Stat6 in $CD4^+$ T cells, had increased C17orf59 expression when compared with $CD4^+$ T cells from $Stat6VT^-$ littermates (Figures 7N and 7O).

DISCUSSION

Here, we report the discovery of an important role of Tregs in maintaining AT function in response to environmental or systemic challenges. Specifically, we demonstrate that cold exposure, physiological levels of beta-adrenergic stimulation, or short-term exposure to a high-caloric challenge each enhances $Foxp3^+$ Tregs and their induction in BAT.

To determine whether the observed Treg-adipose crosstalk in BAT includes a functional programming of BAT-residing T cells, we utilized UCP1ko mice as a BAT loss-of-function model and found that local Treg induction was reduced. Specifically, these findings document that the local AT environment can co-opt local T cell differentiation programs and thereby influence tissue function and organismal homeostasis.

We used loss- and gain-of-function studies, including Treg depletion, transfer, and *in vivo* expansion, to demonstrate an important role of $Foxp3^+$ Tregs for AT function including efficient thermogenesis and lipolysis. Further, the Treg-expansion data implicate a critical function of $Foxp3^+$ Tregs in beiging/browning of white fat.

We further found that a T cell-specific Stat6/Pten axis is a key mechanistic link between environmental challenges, induction of $Foxp3^+$ Treg cells, and AT function. The involvement of Stat6 in $Foxp3^+$ Treg induction has been linked with the IL-2-Stat5 signaling pathway. IL-2R signals can induce IL-4 production through Stat5 (Zhu et al., 2003) or c-Maf activation (Hwang et al., 2002). The IL-4/Stat6/c-Maf/CD25 and IL-2/CD25/c-Maf/IL-4 pathways may converge to act on $CD4^+CD25^{++}Foxp3^+$ Tregs (Sanchez-Guajardo et al., 2007). One possibility to explain the increase in peripheral $Foxp3^+$ Tregs in mice with constitutively active Stat6 in T cells ($Stat6VT^+$ mice) might be improved Treg cell survival by using common downstream elements of the IL-2 pathways (Sanchez-Guajardo et al., 2007). In addition, IL-4, which promotes Stat6 activation (Quelle et al., 1995), can prevent apoptosis of $CD25^{++}Foxp3^+$ Tregs (Maerten et al., 2005). It has been hypothesized that in the periphery, Stat6

(H and I) qRT-PCR analyses of *Borcs6* mRNA abundance in $CD4^+$ T cells purified from mice after (H) *in vivo* ADRB3 stimulation or (I) cold exposure. n = 5 mice per group.

(J) Ratios of *Borcs6*/*Cd4* mRNA abundance in BAT from Stat6ko mice upon NaCl versus CL treatment. n = 4 per group.

(K) *Ex vivo* Treg frequencies purified from BAT of young WT or $Borcs6^{+/-}$ mice upon stimulation with CL (2 days, 1 mg/kg i.p.). n = 3–4 per group.

Data are presented as box-and-whisker plots with min and max values for data distribution. *$p < 0.05$, **$p < 0.01$.

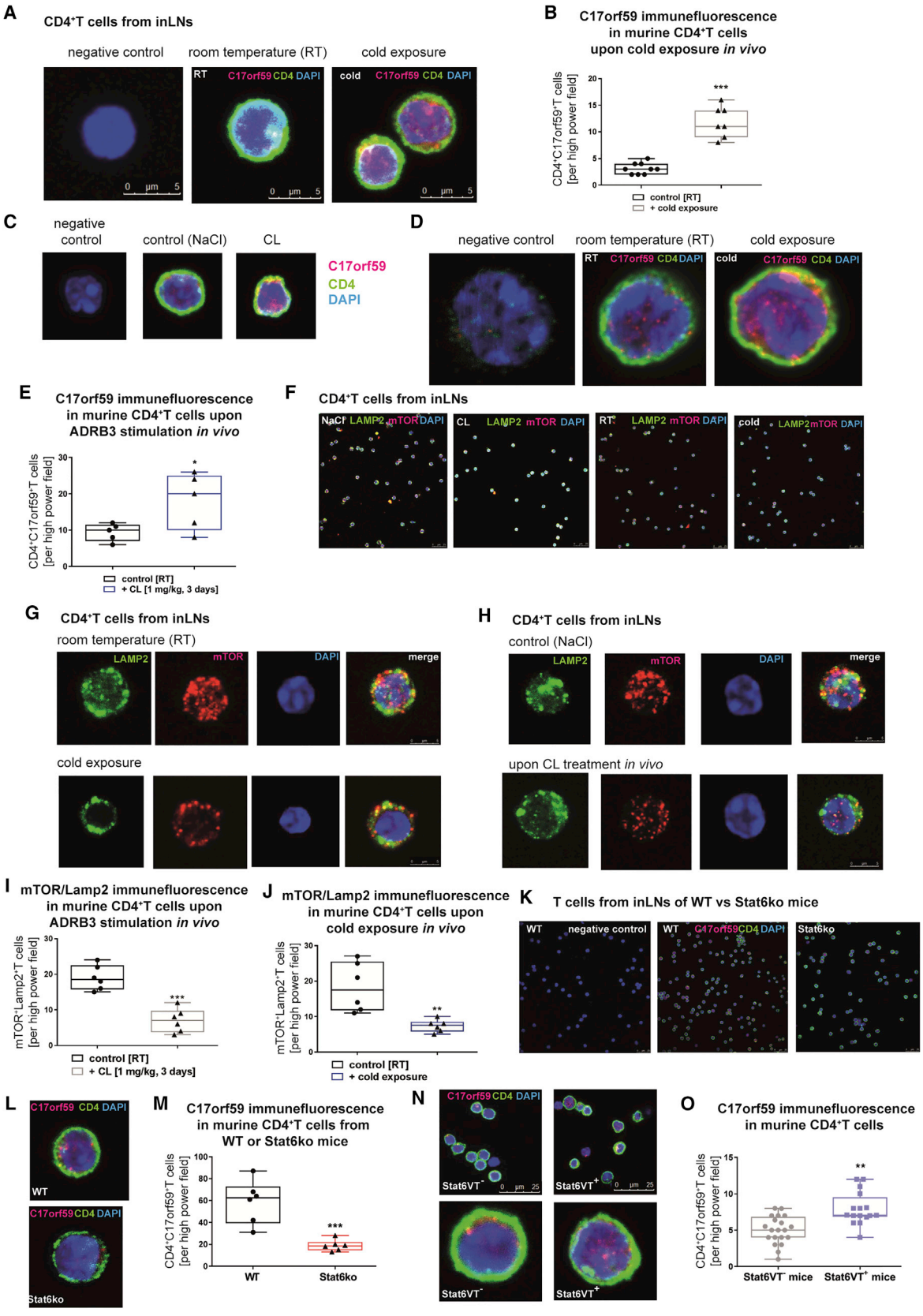

(legend on next page)

does not replace IL-2 signals but rather acts in synergy to enhance Treg survival (Sanchez-Guajardo et al., 2007).

We found that cold exposure or beta3-adrenergic stimulation induces Stat6 phosphorylation in $CD4^+$ T cells, thereby further integrating these environmental stimuli with induction of Stat6 signaling and $Foxp3^+$ Treg induction. Treg abundance and induction, especially in BAT and scWAT, were impaired in the absence of Stat6. These results further integrate with *in vivo* T cell transfer experiments using Stat6-deficient T cells with or without beta3 adrenergic stimulation. These data indicate that Treg induction is impaired intrinsically in the absence of Stat6 and that beta3-adrenergic stimulation does not favor Treg induction in T cells deficient for Stat6.

The role of Stat6 in Treg induction upon cold exposure or beta3-adrenergic stimulation was confirmed in an unbiased T cell proteomics setting. Specifically, in the absence of Stat6 upon ADRB3 stimulation *in vivo*, we observed a downregulation of tolerogenic protein signatures including Foxp3. These immunological data on the reduction of Treg induction in Stat6-deficient animals integrate with metabolic analyses of fat depots from Stat6ko mice. In contrast to what occurs in WT mice upon ADRB3 stimulation *in vivo*, Stat6ko mice have a reduced expression of markers relevant for adipogenesis such as *Adipsin*, and for adipocyte differentiation such as *Pparg* and *P2rx5*. Together with the results from Treg gain- and loss-of-function studies, these findings support a role of $Foxp3^+$ Tregs in affecting AT function.

As one possible means to further interlink Stat6-relevant signaling intermediates, Pten-overexpressing mice had decreased phosphorylated Akt as well as phosphorylated Foxo1 levels together with a significant enhancement of UCP1 expression in BAT (Ortega-Molina et al., 2012). Molecular analyses, including PI3K inhibitors, underscored that the effects of Pten on BAT are mediated by the PI3K/Akt/Foxo signaling pathway that results in the activation of UCP1 and its transcriptional regulator, Ppargc1a (Ortega-Molina et al., 2012).

Our findings linking BAT function with Treg induction are consistent with reports that inhibition of the PI3K/Akt pathway enhances $Foxp3^+$ Treg induction (Daniel and von Boehmer, 2011; Sauer et al., 2008). Regulation of Foxo transcriptional activity is mainly dependent on the phosphorylation of Foxo proteins via the PI3K/Akt pathway. Furthermore, using our unbiased proteomic approach, we identified a series of proteins involved in negative regulation of immune responses as well as Treg induction, frequency, and function. Accordingly, we observed regulation of networks that have an impact on Foxp3 itself as well as its interacting partners. Previous analyses indicated that Foxp3 forms large transcriptional complexes comprising several hundred partners (Rudra et al., 2012). Moreover, upon cold exposure or ADRB3 stimulation, we observed upregulation of Foxp3-associated factors implicated in transcription regulation including Bc11b, CBFβ, and Runx1. Besides being controlled by Foxp3, some of these Foxp3-bound transcription factors also regulate Foxp3 gene expression by binding to its promoter and intronic enhancers (Rudra et al., 2012).

Consistent with these observations, we found C17orf59 to be one of the more prominently enhanced proteins identified in $CD4^+$ T cell proteomes of mice subjected to cold or ADRB3 stimulation. C17orf59 was recently demonstrated to function as a Ragulator-interacting protein that regulates mTORC1 activity through its interaction with Ragulator at the lysosome (Schweitzer et al., 2015). Overexpression of C17orf59 disrupts the Rag-Ragulator complex, prevents Rag lysosomal localization, and thereby inhibits mTORC1 activity (Schweitzer et al., 2015). Inhibition of mTORC1 activity, as demonstrated by established drugs such as rapamycin or everolimus, directly induces $Foxp3^+$ Tregs (Daniel et al., 2010; Sauer et al., 2008; von Boehmer and Daniel, 2013). The increased C17orf59 protein abundance in $CD4^+$ T cells of mice subjected to cold or ADRB3 stimulation supports a concept in which physiological levels of ADRB3 stimulation can exert mTORC1-inhibiting activity, thereby directly contributing to the induction of $Foxp3^+$ Tregs. To integrate the findings on the role of Stat6 for T cell tolerance induction, C17orf59 protein expression in $CD4^+$ T cells from Stat6ko animals was not identified under steady-state conditions or following beta3-adrenergic stimulation.

In sum, we demonstrate that local $Foxp3^+$ Treg induction in AT in response to environmental stimuli such as cold or a

Figure 7. Treg Accumulation in Adipose Tissue by Cold Exposure or ADRB3 Stimulation Involves C17orf59/Borcs6

(A) Representative confocal microscopy images for C17orf59 expression of $CD4^+$ T cells purified from inLNs of mice exposed to cold *in vivo* (24 hr, 4°C). Scale bar, 5 μm.

(B) $C17orf59^+CD4^+$ T cells per high power field in samples from $CD4^+$ T cells from (A). n = 9 for control group at room temperature and n = 6 for group at 4°C.

(C) Representative high-magnification confocal images for C17orf59 expression of $CD4^+$ T cells purified from inLNs of mice subjected to ADRB3 stimulation (3 days, 1 mg/kg CL).

(D) $C17orf59^+CD4^+$ T cells per high power field in samples from (C). n = 5 per group.

(E) Stimulated emission depletion microscopy of cytoplasmic C17orf59 expression in $CD4^+$ T cells purified from inLNs of mice upon cold exposure.

(F) Representative confocal microscopy images for Lamp2 and mTOR expression in $CD4^+$ T cells purified from inLNs of mice subjected to ADRB3 stimulation or cold exposure *in vivo*. Scale bar, 25 μm.

(G and H) Single-cell magnifications and depiction of single stainings of samples from (F) after cold exposure (G) or ADRB3 stimulation (H). Scale bar, 5 μm.

(I) $mTOR^+Lamp2^+$ T cells per high power field in samples from $CD4^+$ T cells purified from inLNs of mice subjected to CL (3 days, 1 mg/kg CL). n = 6 per group.

(J) $mTOR^+Lamp2^+$ T cells per high power field from $CD4^+$ T cells purified from inLNs of mice subjected to cold exposure (24 hr, 4°C) *in vivo*. n = 6 per group.

(K) Left: negative staining control of C17orf59. Shown are stainings with secondary antibody in the absence of primary antibodies using $CD4^+$ T cells from WT mice. Middle and right: representative confocal microscopy overview images for C17orf59 expression in $CD4^+$ T cells purified from inLNs of WT or BALB/c Stat6ko mice. Scale bar, 25 μm.

(L) Representative confocal microscopy images for C17orf59 expression in $CD4^+$ T cells purified from inLNs of WT or BALB/c Stat6ko mice.

(M) Quantification of C17orf59 immunofluorescence of murine $CD4^+$ T cells from WT or Stat6ko mice.

(N and O) Representative confocal microscopy images for C17orf59 abundance in $CD4^+$ T cells from $Stat6VT^-$ versus $Stat6VT^+$ mice (N) and the corresponding quantification (O). Scale bar, 25 μm.

Data are presented as box-and-whisker plots with min and max values for data distribution. $^*p < 0.05$, $^{**}p < 0.01$, $^{***}p < 0.001$.

high-caloric challenge, or direct beta3-adrenergic stimulation, involves Stat6/Pten signaling. These findings are consistent with recently emerging hypotheses that local metabolic changes can link gene regulation, signaling, differentiation, and function in order to drive tissue-specific T cell differentiation and fate (Panduro et al., 2016). These novel insights into the molecular underpinnings of tissue-specific Treg induction uncover their role in linking environmental influences with adipose function and metabolic diseases. Our discoveries suggest the potential for tailored anti-inflammatory interventions aimed toward restoring AT homeostasis.

STAR★METHODS

Detailed methods are provided in the online version of this paper and include the following:

- KEY RESOURCES TABLE
- CONTACT FOR REAGENT AND RESOURCE SHARING
- EXPERIMENTAL MODEL AND SUBJECT DETAILS
  - Mice
  - *In Vitro* Studies with Primary Murine T Cells
- METHOD DETAILS
  - Isolation of $CD4^+$T Cells from Lymphoid Organs
  - Isolation of $CD4^+$T Cells from Adipose Tissues
  - Cell Staining for Flow Cytometry
  - *In vitro* Treg-Induction Assay
  - Chemicals and Enzymes Used for Experiments
  - Quantitative Analysis of mRNA Abundance
  - Proteomics
  - Immunefluorescence by Confocal Microscopy
  - Immunofluorescence by STED Microscopy
- QUANTIFICATION AND STATISTICAL ANALYSIS
- DATA AND SOFTWARE AVAILABILITY
  - Data Resources

SUPPLEMENTAL INFORMATION

Supplemental Information includes five figures and one table and can be found with this article online at http://dx.doi.org/10.1016/j.cmet.2017.08.008.

AUTHOR CONTRIBUTIONS

S. Kälin and M. Becker performed experiments, analyzed data, and wrote the manuscript. V.B.O. performed analyses of AT function. I.S. performed *in vivo* experiments. L.F.R.N. performed *in vitro* experiments. M.M.H.M. and V.K.F. performed *in vitro* experiments. M.G.S. performed Treg induction analyses. S. Keipert supported BAT analyses. D.L. supported T cell analyses. F.R.-J. provided beta-less mice and supported analyses of animals. K.G. and V.P. analyzed T cells. M.H.K. and P.K. provided Stat6VT mice and supported analyses of mice. M.J. supported analyses of BAT tissues. F.H. performed proteomic profiling of $CD4^+$ T cells. M.S. provided PtenTg mice and supported analyses of animals. M. Blüher supported analyses of AT function. S.D. supported experiments with Foxp3 DTR mice. T.B. provided Foxp3 DTR mice. C.W. performed experiments with *in vivo* cold exposure. P.T. and R.P. performed STED microscopy and related analyses. B.W. performed gain- and loss-of-function experiments for Treg analyses, immunofluorescence, and confocal microscopy. S.C.W. contributed to the writing of the manuscript. A.-G.Z. contributed to conceptualization and discussion of the project. M.M. supervised proteomic analyses. M.H.T. provided substantial conceptualization and contributed to writing of the manuscript. C.D. conceptualized, designed, and performed *in vivo* experiments; analyzed and interpreted data; and wrote the manuscript.

ACKNOWLEDGMENTS

The authors thank Siegfried Ussar for helpful discussions, Michael Pfaffl, and the EMBL Genecore facility and its personnel, especially Vladimir Benes, for providing reagents, materials, and analysis tools for NGS. V.B.O. is supported by Technische Universität München – Institute for Advanced Study, funded by the German Excellence Initiative and the European Union Seventh Framework Programme under grant agreement n° 291763. C.D. is supported by a Research Group at Helmholtz Zentrum München and the German Center for Diabetes Research (DZD) and received support through a membership in the CRC1054 of the Deutsche Forschungsgemeinschaft (B11). M.H.K. is supported by a Public Health Services award (AI095282). B.W. is supported by WE 4656/2 and DFG-CRC1181 (B02). R.P. and P.T. (OICE) are supported by DFG-CRC1181 (Z02). M.H.T. received support from the Alexander von Humboldt Foundation, the DZD, the Helmholtz Alliance ICEMED, and the Helmholtz Initiative on Personalized Medicine *iMed* by Helmholtz Association, and the Helmholtz cross-program topic "Metabolic Dysfunction."

Received: July 29, 2016
Revised: July 21, 2017
Accepted: August 8, 2017
Published: September 5, 2017

REFERENCES

Anders, S., Pyl, P.T., and Huber, W. (2015). HTSeq–a Python framework to work with high-throughput sequencing data. Bioinformatics *31*, 166–169.

Andrews, S. (2010). FastQC: a quality control tool for high throughput sequence data. (Babraham Bioinformatics). http://www.bioinformatics.babraham.ac.uk/projects/fastqc.

Bachman, E.S., Dhillon, H., Zhang, C.-Y., Cinti, S., Bianco, A.C., Kobilka, B.K., and Lowell, B.B. (2002). βAR signaling required for diet-induced thermogenesis and obesity resistance. Science *297*, 843–845.

Bapat, S.P., Myoung Suh, J., Fang, S., Liu, S., Zhang, Y., Cheng, A., Zhou, C., Liang, Y., LeBlanc, M., Liddle, C., et al. (2015). Depletion of fat-resident Treg cells prevents age-associated insulin resistance. Nature *528*, 137–141.

Bruns, H.A., Schindler, U., and Kaplan, M.H. (2003). Expression of a constitutively active stat6 in vivo alters lymphocyte homeostasis with distinct effects in T and B cells. J. Immunol. *170*, 3478–3487.

Chang, C.H., and Pearce, E.L. (2016). Emerging concepts of T cell metabolism as a target of immunotherapy. Nat. Immunol. *17*, 364–368.

Chapoval, S., Dasgupta, P., Dorsey, N.J., and Keegan, A.D. (2010). Regulation of the T helper cell type 2 (Th2)/T regulatory cell (Treg) balance by IL-4 and STAT6. J. Leukoc. Biol. *87*, 1011–1018.

Cipolletta, D., Feuerer, M., Li, A., Kamei, N., Lee, J., Shoelson, S.E., Benoist, C., and Mathis, D. (2012). PPAR-gamma is a major driver of the accumulation and phenotype of adipose tissue Treg cells. Nature *486*, 549–553.

Cipolletta, D., Cohen, P., Spiegelman, B.M., Benoist, C., and Mathis, D. (2015). Appearance and disappearance of the mRNA signature characteristic of Treg cells in visceral adipose tissue: age, diet, and PPARgamma effects. Proc. Natl. Acad. Sci. USA *112*, 482–487.

Cox, J., Hein, M.Y., Luber, C.A., Paron, I., Nagaraj, N., and Mann, M. (2014). Accurate proteome-wide label-free quantification by delayed normalization and maximal peptide ratio extraction, termed MaxLFQ. Mol. Cell. Proteomics *13*, 2513–2526.

Cox, J., and Mann, M. (2008). MaxQuant enables high peptide identification rates, individualized p.p.b.-range mass accuracies and proteome-wide protein quantification. Nat. Biotechnol. *26*, 1367–1372.

Cox, J., Neuhauser, N., Michalski, A., Scheltema, R.A., Olsen, J.V., and Mann, M. (2011). Andromeda: a peptide search engine integrated into the MaxQuant environment. J. Proteome Res. *10*, 1794–1805.

Cypess, A.M., White, A.P., Vernochet, C., Schulz, T.J., Xue, R., Sass, C.A., Huang, T.L., Roberts-Toler, C., Weiner, L.S., Sze, C., et al. (2013). Anatomical localization, gene expression profiling and functional characterization of adult human neck brown fat. Nat. Med. *19*, 635–639.

Daniel, C., and von Boehmer, H. (2011). Extrathymic generation of regulatory T cells–chances and challenges for prevention of autoimmune disease. Adv. Immunol. *112*, 177–213.

Daniel, C., Wennhold, K., Kim, H.J., and von Boehmer, H. (2010). Enhancement of antigen-specific Treg vaccination in vivo. Proc. Natl. Acad. Sci. USA *107*, 16246–16251.

Daniel, C., Weigmann, B., Bronson, R., and von Boehmer, H. (2011). Prevention of type 1 diabetes in mice by tolerogenic vaccination with a strong agonist insulin mimetope. J. Exp. Med. *208*, 1501–1510.

Fedorenko, A., Lishko, P.V., and Kirichok, Y. (2012). Mechanism of fatty-acid-dependent UCP1 uncoupling in brown fat mitochondria. Cell *151*, 400–413.

Feldmann, H.M., Golozoubova, V., Cannon, B., and Nedergaard, J. (2009). UCP1 ablation induces obesity and abolishes diet-induced thermogenesis in mice exempt from thermal stress by living at thermoneutrality. Cell Metab. *9*, 203–209.

Feuerer, M., Herrero, L., Cipolletta, D., Naaz, A., Wong, J., Nayer, A., Lee, J., Goldfine, A.B., Benoist, C., Shoelson, S., et al. (2009). Lean, but not obese, fat is enriched for a unique population of regulatory T cells that affect metabolic parameters. Nat. Med. *15*, 930–939.

Gessner, A., Mohrs, K., and Mohrs, M. (2005). Mast cells, basophils, and eosinophils acquire constitutive IL-4 and IL-13 transcripts during lineage differentiation that are sufficient for rapid cytokine production. J. Immunol. *174*, 1063–1072.

Goenka, S., and Kaplan, M.H. (2011). Transcriptional regulation by STAT6. Immunol. Res. *50*, 87–96.

Gottschalk, R.A., Corse, E., and Allison, J.P. (2010). TCR ligand density and affinity determine peripheral induction of Foxp3 in vivo. J. Exp. Med. *207*, 1701–1711.

Guillot, X., Tordi, N., Mourot, L., Demougeot, C., Dugue, B., Prati, C., and Wendling, D. (2014). Cryotherapy in inflammatory rheumatic diseases: a systematic review. Expert Rev. Clin. Immunol. *10*, 281–294.

Heng, T.S., and Painter, M.W.; Immunological Genome Project Consortium (2008). The immunological genome project: networks of gene expression in immune cells. Nat. Immunol. *9*, 1091–1094.

Hwang, E.S., White, I.A., and Ho, I.C. (2002). An IL-4-independent and CD25-mediated function of c-maf in promoting the production of Th2 cytokines. Proc. Natl. Acad. Sci. USA *99*, 13026–13030.

Kaplan, M.H., Schindler, U., Smiley, S.T., and Grusby, M.J. (1996). Stat6 is required for mediating responses to IL-4 and for the development of Th2 cells. Immunity *4*, 313–319.

Kim, C.H. (2007). Molecular targets of FoxP3+ regulatory T cells. Mini Rev. Med. Chem. *7*, 1136–1143.

Kim, J.M., Rasmussen, J.P., and Rudensky, A.Y. (2007). Regulatory T cells prevent catastrophic autoimmunity throughout the lifespan of mice. Nat. Immunol. *8*, 191–197.

Klimek, A.T., Lubkowska, A., Szygula, Z., Fraczek, B., and Chudecka, M. (2011). The influence of single whole body cryostimulation treatment on the dynamics and the level of maximal anaerobic power. Int. J. Occup. Med. Environ. Health *24*, 184–191.

Kretschmer, K., Apostolou, I., Hawiger, D., Khazaie, K., Nussenzweig, M.C., and von Boehmer, H. (2005). Inducing and expanding regulatory T cell populations by foreign antigen. Nat. Immunol. *6*, 1219–1227.

Kulak, N.A., Pichler, G., Paron, I., Nagaraj, N., and Mann, M. (2014). Minimal, encapsulated proteomic-sample processing applied to copy-number estimation in eukaryotic cells. Nat. Methods *11*, 319–324.

Lewis, M., Tarlton, J.F., and Cose, S. (2008). Memory versus naive T-cell migration. Immunol. Cell Biol. *86*, 226–231.

Li, H., Handsaker, B., Wysoker, A., Fennell, T., Ruan, J., Homer, N., Marth, G., Abecasis, G., and Durbin, R.; 1000 Genome Project Data Processing Subgroup (2009). The sequence Alignment/Map format and SAMtools. Bioinformatics *25*, 2078–2079.

Love, M.I., Huber, W., and Anders, S. (2014). Moderated estimation of fold change and dispersion for RNA-seq data with DESeq2. Genome Biol. *15*, 550.

Lubkowska, A., Szygula, Z., Chlubek, D., and Banfi, G. (2011). The effect of prolonged whole-body cryostimulation treatment with different amounts of sessions on chosen pro- and anti-inflammatory cytokines levels in healthy men. Scand. J. Clin. Lab. Invest. *71*, 419–425.

MacIver, N.J., Michalek, R.D., and Rathmell, J.C. (2013). Metabolic regulation of T lymphocytes. Annu. Rev. Immunol. *31*, 259–283.

Maerten, P., Shen, C., Bullens, D.M., Van Assche, G., Van Gool, S., Geboes, K., Rutgeerts, P., and Ceuppens, J.L. (2005). Effects of interleukin 4 on CD25+CD4+ regulatory T cell function. J. Autoimmun. *25*, 112–120.

Mathis, D. (2013). Immunological goings-on in visceral adipose tissue. Cell Metab. *17*, 851–859.

Medrikova, D., Sijmonsma, T.P., Sowodniok, K., Richards, D.M., Delacher, M., Sticht, C., Gretz, N., Schafmeier, T., Feuerer, M., and Herzig, S. (2015). Brown adipose tissue harbors a distinct sub-population of regulatory T cells. PLoS One *10*, e0118534.

Meissner, F., and Mann, M. (2014). Quantitative shotgun proteomics: considerations for a high-quality workflow in immunology. Nat. Immunol. *15*, 112–117.

Ortega-Molina, A., Efeyan, A., Lopez-Guadamillas, E., Munoz-Martin, M., Gomez-Lopez, G., Canamero, M., Mulero, F., Pastor, J., Martinez, S., Romanos, E., et al. (2012). Pten positively regulates brown adipose function, energy expenditure, and longevity. Cell Metab. *15*, 382–394.

Panduro, M., Benoist, C., and Mathis, D. (2016). Tissue Tregs. Annu. Rev. Immunol. *34*, 609–633.

Pillemer, B.B., Qi, Z., Melgert, B., Oriss, T.B., Ray, P., and Ray, A. (2009). STAT6 activation confers upon T helper cells resistance to suppression by regulatory T cells. J. Immunol. *183*, 155–163.

Qiu, Y., Nguyen, K.D., Odegaard, J.I., Cui, X., Tian, X., Locksley, R.M., Palmiter, R.D., and Chawla, A. (2014). Eosinophils and type 2 cytokine signaling in macrophages orchestrate development of functional beige fat. Cell *157*, 1292–1308.

Quelle, F.W., Shimoda, K., Thierfelder, W., Fischer, C., Kim, A., Ruben, S.M., Cleveland, J.L., Pierce, J.H., Keegan, A.D., Nelms, K., et al. (1995). Cloning of murine Stat6 and human Stat6, Stat proteins that are tyrosine phosphorylated in responses to IL-4 and IL-3 but are not required for mitogenesis. Mol. Cell. Biol. *15*, 3336–3343.

Rosen, E.D., and Spiegelman, B.M. (2014). What we talk about when we talk about fat. Cell *156*, 20–44.

Rothwell, N.J., and Stock, M.J. (1979). A role for brown adipose tissue in diet-induced thermogenesis. Nature *281*, 31–35.

Rudra, D., deRoos, P., Chaudhry, A., Niec, R.E., Arvey, A., Samstein, R.M., Leslie, C., Shaffer, S.A., Goodlett, D.R., and Rudensky, A.Y. (2012). Transcription factor Foxp3 and its protein partners form a complex regulatory network. Nat. Immunol. *13*, 1010–1019.

Saito, M., Okamatsu-Ogura, Y., Matsushita, M., Watanabe, K., Yoneshiro, T., Nio-Kobayashi, J., Iwanaga, T., Miyagawa, M., Kameya, T., Nakada, K., et al. (2009). High incidence of metabolically active brown adipose tissue in healthy adult humans: effects of cold exposure and adiposity. Diabetes *58*, 1526–1531.

Sanchez-Guajardo, V., Tanchot, C., O'Malley, J.T., Kaplan, M.H., Garcia, S., and Freitas, A.A. (2007). Agonist-driven development of CD4+CD25+Foxp3+ regulatory T cells requires a second signal mediated by Stat6. J. Immunol. *178*, 7550–7556.

Sauer, S., Bruno, L., Hertweck, A., Finlay, D., Leleu, M., Spivakov, M., Knight, Z.A., Cobb, B.S., Cantrell, D., O'Connor, E., et al. (2008). T cell receptor signaling controls Foxp3 expression via PI3K, Akt, and mTOR. Proc. Natl. Acad. Sci. USA *105*, 7797–7802.

Scheltema, R.A., and Mann, M. (2012). SprayQc: a real-time LC-MS/MS quality monitoring system to maximize uptime using off the shelf components. J. Proteome Res. *11*, 3458–3466.

Schwanhäusser, B., Busse, D., Li, N., Dittmar, G., Schuchhardt, J., Wolf, J., Chen, W., and Selbach, M. (2011). Global quantification of mammalian gene expression control. Nature *473*, 337–342.

Schweitzer, L.D., Comb, W.C., Bar-Peled, L., and Sabatini, D.M. (2015). Disruption of the rag-ragulator complex by c17orf59 inhibits mTORC1. Cell Rep. *12*, 1445–1455.

Sehra, S., Bruns, H.A., Ahyi, A.N., Nguyen, E.T., Schmidt, N.W., Michels, E.G., von Bulow, G.U., and Kaplan, M.H. (2008). IL-4 is a critical determinant in the generation of allergic inflammation initiated by a constitutively active Stat6. J. Immunol. *180*, 3551–3559.

Serr, I., Fürst, R.W., Achenbach, P., Scherm, M.G., Gökmen, F., Haupt, F., Sedlmeier, E.-M., Knopff, A., Shultz, L., Willis, R.A., et al. (2016). Type 1 diabetes vaccine candidates promote human Foxp3+Treg induction in humanized mice. Nat. Commun. *7*, 10991.

Setiady, Y.Y., Coccia, J.A., and Park, P.U. (2010). In vivo depletion of CD4+FOXP3+ Treg cells by the PC61 anti-CD25 monoclonal antibody is mediated by FcgammaRIII+ phagocytes. Eur. J. Immunol. *40*, 780–786.

Shrestha, S., Yang, K., Guy, C., Vogel, P., Neale, G., and Chi, H. (2015). Treg cells require the phosphatase PTEN to restrain TH1 and TFH cell responses. Nat. Immunol. *16*, 178–187.

Tyanova, S. (2016). The Perseus computational platform for comprehensive analysis of (prote)omics data. Nat. Methods *13*, 731–740.

UniProt, C. (2015). UniProt: a hub for protein information. Nucleic Acids Res. *43*, D204–D212.

Vizcaino, J.A., Deutsch, E.W., Wang, R., Csordas, A., Reisinger, F., Rios, D., Dianes, J.A., Sun, Z., Farrah, T., Bandeira, N., et al. (2014). ProteomeXchange provides globally coordinated proteomics data submission and dissemination. Nat. Biotechnol. *32*, 223–226.

von Boehmer, H., and Daniel, C. (2013). Therapeutic opportunities for manipulating T(Reg) cells in autoimmunity and cancer. Nat. Rev. Drug Discov. *12*, 51–63.

Webster, K.E., Walters, S., Kohler, R.E., Mrkvan, T., Boyman, O., Surh, C.D., Grey, S.T., and Sprent, J. (2009). In vivo expansion of T reg cells with IL-2-mAb complexes: induction of resistance to EAE and long-term acceptance of islet allografts without immunosuppression. J. Exp. Med. *206*, 751–760.

Yu, X.Y., Lin, S.G., Wang, X.M., Liu, Y., Zhang, B., Lin, Q.X., Yang, M., and Zhou, S.F. (2007). Evidence for coexistence of three beta-adrenoceptor subtypes in human peripheral lymphocytes. Clin. Pharmacol. Ther. *81*, 654–658.

Zhu, J., Cote-Sierra, J., Guo, L., and Paul, W.E. (2003). Stat5 activation plays a critical role in Th2 differentiation. Immunity *19*, 739–748.

STAR★METHODS

KEY RESOURCES TABLE

REAGENT or RESOURCE	SOURCE	IDENTIFIER
Antibodies		
CD4 Biotin	BioLegend	Clone: GK1.5; Cat# 553728; RRID: AB_395012
CD8a Pacific Blue	BioLegend	Clone: 53-6.7; Cat# 100725; RRID: AB_493425
CD11b Pacific Blue	BioLegend	Clone: M1/70; Cat# 101224; RRID: AB_755986
CD11c Brilliant Violett 421	BioLegend	Clone: N418; Cat# 117330; RRID: AB_11219593
B220 Pacific Blue	BioLegend	Clone: RA3-6B2; Cat# 103227; RRID: AB_492876
F4/80 Pacific Blue	BioLegend	Clone: BM8; Cat# 123124; RRID: AB_893475
CD25 PerCP-Cy5.5	BioLegend	Clone: PC61; Cat# 102030; RRID: AB_893288
CD44 PE	BioLegend	Clone: IM7; Cat# 103008; RRID: AB_312959
Ki67 APC	BioLegend	Clone: 16A8; Cat# 652406; RRID: AB_2561930
Ki67 Brilliant Violett 605	BioLegend	Clone: 16A8; Cat# 652413; RRID: AB_2562664
CD4 Alexa Fluor 700	eBioscience	Clone: RM4-5; Cat# 56-0042-82; RRID: AB_494000
CD62L APC	eBioscience	Clone: MEL-14; Cat# 17-0621-82; RRID: AB_469410
Foxp3 FITC	eBioscience	Clone: FJK-16s; Cat# 11-5773-82; RRID: AB_465243
CD14 V450	BD Biosciences	Clone: rmC5-3; Cat# 560639; RRID: AB_1727429
CD90.1 PerCP-Cy5.5	BioLegend	Clone: OX-7; Cat# 202515; RRID: AB_961438
CD90.2 APC-Cy7	BioLegend	Clone: 30-H12; Cat#105328; RRID: AB_10613293
Anti-mouse CD25 (mCD25)	BioXCell	Clone: PC-61.5.3; Cat# BE0012; RRID: AB_1107619
Fc-Block	BD Pharmingen	Clone: 2.4G2; Cat# 553142; RRID: AB_394657
CD3e	BD Pharmingen	Clone: 145-2C11; Cat# 553057; RRID: AB_394590
CD28	BD Pharmingen	Clone: 37.51; Cat# 553294; RRID: AB_394763
p-Stat6 (pY641) Alexa Fluor 647	BD Phosflow™	Clone: J71-773.58.11; Cat# 558242; RRID: AB_647145
p-Stat6 rabbit anti-mouse	Cell Signaling	Cat# 9361S; RRID: AB_331595
anti-mouse IL-2	eBioscience	Clone: JES6-1A12; Cat# 16-7022-85; RRID: AB_469207
rabbit anti-mouse C17orf59	MyBioSource	polyclonal; Cat# MBS6004199; RRID: N/A
mouse anti-mouse Stat6	Cell Signaling	polyclonal; Cat# 9362; RRID: AB_2271211
rat-anti-mouse LAMP2	BioLegend	Clone: M3/84; Cat# 108502; RRID: AB_313383
Mouse anti-mTOR	Thermo Fisher Scientific	Clone: 215Q18; Cat# AHO1232; RRID: AB_2536329
Hamster anti-mouse CD3	BioLegend	Clone: 145-2C11; Cat# 100302; RRID: AB_312667
Rat anti-mouse CD4	BioLegend	Clone: RM4-5; Cat #100506; RRID: AB_312709
Rat anti-mouse CD4	eBioscience	Clone: GK1.5; Cat# 14-0041-8; RRID: AB_467064
$F(ab')_2$ donkey anti-rabbit IgG PE	eBioscience	polyclonal; Cat# 12-4739-81; RRID: AB_1210761
goat anti-rat Alexa Fluor 488	Life Technologies	polyclonal; Cat #A11006; RRID: AB_2534074
biotinylated goat-anti- armen. hamster IgG	eBioscience	polyclonal; Cat #13-4113-85; RRID: AB_466651
donkey-anti-mouse AlexaFluor 555	Life Technologies	polyclonal; Cat# A-31570; RRID: AB_2536180
goat-anti-mouse Cy3	Dianova	polyclonal; Cat# 115-165-146; RRID: AB_2491007
goat-anti-rat AlexaFluor 594	Life Technologies	polyclonal; Cat#A11007; RRID: AB_141374
goat anti-rabbit AlexaFluor 594	Life Technologies	polyclonal; Cat# A11012; RRID: AB_141359
rat-anti-mouse biotinylated	Dianova	polyclonal; Cat# 415-065-166; RRID: AB_2340272
horse anti-rabbit biotinylated	Vector Laboratory	Cat# BA-1100; RRID: AB_2336201
goat-anti-rat STAR580	abberior	Cat# 2-0132-005-1; RRID: N/A
goat-anti-rabbit STAR635P	abberior	Cat# 2-0132-005-5; RRID: N/A
Chemicals, Peptides, and Recombinant Proteins		
Foxp3 Staining Buffer Set	eBioscience	Cat# 00-5523-00
Fixable Viability Dye eFluor450	eBioscience	Cat# 65-0863-18

(*Continued on next page*)

Continued

REAGENT or RESOURCE	SOURCE	IDENTIFIER
Sytox Red	Thermo Fisher Scientific	Cat# S34859
Sytox Blue	Thermo Fisher Scientific	Cat# S34857
Streptavidin Microbeads	Miltenyi	Cat #130-048-101
Dynabeads untouched CD4+ mouse	Invitrogen	Cat# 11415D
Streptavidin Alexa Fluor 488	Dianova	Cat# 016-540-084
Streptavidin Dylight 549	Vector Laboratory	Cat# SA-5549
Streptavidin Pacific Blue	Invitrogen	Cat# S11222
Hoechst 33342 dye	Invitrogen	Cat # H1399; CAS 23491-52-3
high fat high sugar (HFHS) diet	Research Diets	Cat# D12331
Pten Inhibitor SF1670	Abcam	Cat# ab141303; CAS 345630-40-2
Stat6 Inhibitor AS 1517499	Axon Medchem	Cat# Axon 1992 ; CAS 919486-40-1
CL-316243	Sigma Aldrich	Cat# C5976; CAS 138908-40-4
cyanopindolol hemifumarate	Tocris	Cat#0993; CAS 69906-86-1
LysC	Wako Chemicals	Cat# 129-02541; EC# 3.4.21.50
trypsin	Sigma Aldrich	Cat# T6567; EC# 232-650-8
ReproSil-Pur C18-AQ 1.9 μm resin	Dr. Maisch GmbH	Cat# R119.b9
Roti-Histofix 4%	Carl Roth	Cat# P087.5
Ficoll-Paque PLUS	GE Healthcare	Cat# 17-1440-03
recombinant human IL-2	ReproTech	Cat# 200-02
collagenase type II	Sigma Aldrich	Cat#C6885; EC #3.4.24.3
collagenase D	Roche	Cat#11088882001; EC #3.4.24.3
Critical Commercial Assays		
miRNeasy Micro Kit	Qiagen	Cat# 217084
Eva Green SuperMix	BioRad	Cat# 1725202
iScript Advanced cDNA Synthesis Kit	BioRad	Cat# 1725038
SMARTer ultra-low input RNA Kit for sequencing – v4	Takara Clonetech	Cat# 634890
SMARTer Universal Low Input RNA Kit for Sequencing	Takara Clonetech	Cat# 634889
Deposited Data		
mass spectrometry data	This paper	ProteomeXchange Consortium via PRIDE repository; Identifier: ProteomeXchange: PXD004671
Experimental Models: Organisms/Strains		
CD90.1 Balb/c; genotype: CBy.PL(B6)-*Thy1*^{a}/ScrJ	Jackson Laboratory	RRID: IMSR_JAX:005443
CD90.2 Balb/c; genotype: Balb/cByJ	Jackson Laboratory	RRID: IMSR_JAX:001026
Foxp3 GFP Balbc; genotype: C.Cg-Foxp3^{tm2Tch}/J	Jackson Laboratory	RRID: IMSR_JAX:006769
Foxp3 GFP Bl6; genotype: B6.Cg-Foxp3^{tm2Tch}/J	Jackson Laboratory	RRID: IMSR_JAX:006772
Stat6VT+ Bl6; genotype: Stat6 VT/AA mutation	Mark H. Kaplan, Indiana University, USA (Bruns et al., 2003)	N/A
Stat6KO Balbc; genotype: C.129S2-*Stat6*^{tm1Gru}/J	Mark H. Kaplan, Indiana University, USA (Kaplan et al., 1996)	RRID: IMSR_JAX:002828
Stat6KO 4get-GFP, Balbc	Benno Weigmann, University Erlangen, Germany (Gessner et al., 2005)	N/A
PtenTg Bl6	Manuel Serrano, Spanish National Cancer Research Center, Spain (Ortega-Molina et al., 2012)	N/A
Betaless; genotype: Adrb1,2,3TKO	Francoise Rohner-Jeanrenaud, University of Geneva, Switzerland	N/A

(*Continued on next page*)

Continued		
REAGENT or RESOURCE	SOURCE	IDENTIFIER
Borcs6$^{+/-}$; genotype: B6N(Cg)-*Borcs6$^{tm1.1(KOMP)Vlcg}$*/J	Jackson Laboratory	RRID: IMSR_JAX:028178
Humanized mice; genotype: *NOD.Cg-Prkdc^{scid} H2-Ab1^{tm1Gru} Il2rg^{tm1Wjl}* Tg(HLA-DQA1,HLA-DQB1)1Dv//Sz	Leonard Shultz, Jackson Laboratory	N/A
Foxp3-DTR; genotype: C57BL/6-Tg(Foxp3-DTR/EGFP)23.2Spar/Mmjax	Tobias Bopp, Johannes Gutenberg University Mainz, Germany	RRID: MMRRC_032050-JAX
Sequence-Based Reagents		
Custom primers used for qPCR	This paper	Table S1
Software and Algorithms		
FlowJo software (version 7.6.1)	TreeStar, OR	https://www.flowjo.com/solutions/flowjo/downloads/
FACSDiva software (version 6.1.3)	Beckton Dickinson	N/A
Prism (version 6.0.1)	GraphPad	https://www.graphpad.com/scientific-software/prism/
Statistical Package for the Social Sciences (SPSS) (version 19.0)	IBM	https://www-01.ibm.com/software/de/analytics/spss/download/
SprayQc software	(Scheltema and Mann, 2012)	http://sprayqc.sourceforge.net/
MaxQuant software package (version 1.5.3.29)	(Cox and Mann, 2008)	http://www.coxdocs.org/doku.php?id=maxquant:start
Andromeda search engine	(Cox et al., 2011)	http://www.coxdocs.org/doku.php?id=maxquant:andromeda:start
iBAQ algorithm	(Schwanhäusser et al., 2011)	N/A
Perseus software package	(Tyanova, 2016)	http://www.coxdocs.org/doku.php?id=perseus:common:download_and_installation
DESeq2	(Love et al., 2014)	https://bioconductor.org/packages/release/bioc/html/DESeq2.html
SAMTools	(Li et al., 2009)	N/A
FastQC	(Andrews, 2010)	http://www.bioinformatics.babraham.ac.uk/projects/fastqc
HTSeq-count	(Anders et al., 2015)	http://www-huber.embl.de/users/anders/HTSeq/doc/install.html

CONTACT FOR REAGENT AND RESOURCE SHARING

Further information and requests for resources and reagents should be directed to and will be fulfilled by the Lead Contact, Matthias Tschöp (tschoep@helmholtz-muenchen.de).

EXPERIMENTAL MODEL AND SUBJECT DETAILS

Mice

CBy.PL(B6)-*Thy1^{a}*/ScrJ (CD90.1 BALB/c), Balb/cByJ (CD90.2 BALB/c), heterozygous B6N(Cg)-*Borcs6$^{tm1.1(KOMP)Vlcg}$*/J (Borcs6$^{+/-}$), C.Cg-Foxp3^{tm2Tch}/J (Foxp3-GFP BALB/c) and B6.Cg-Foxp3^{tm2Tch}/J mice (Foxp3-GFP Bl6) mice were originally obtained from Jackson Laboratories. C.129S2-*Stat6^{tm1Gru}*/J (Kaplan et al., 1996), referred to as Stat6ko mice, and Stat6VT mice (Bruns et al., 2003) were previously described. Pten Tg Bl6 mice were kindly provided by Manuel Serrano (Spanish National Cancer Research Center (CNIO), Spain). Adrb1,2,3TKO mice, referred to as betaless mice, were kindly provided by Francoise Rohner-Jeanrenaud (Faculty of Medicine, University of Geneva, Switzerland). Humanized mice, *NOD.Cg-Prkdc^{scid} H2-Ab1^{tm1Gru} Il2rg^{tm1Wjl}* Tg(HLA-DQA1,HLA-DQB1)1Dv//Sz mice, lack murine MHC class II and transgenically express human HLA-DQ8. These mice were developed by Leonard Shultz at the Jackson Laboratory. For the high-caloric challenge, mice were fed *ad libitum* with a high-fat, high-sugar (HFHS) diet composed of 58.0% kcal from fat, 25.5% kcal from carbohydrates (including 8% sucrose) and 16.4% kcal from protein (Research Diets, #D12331, New Brunswick, NJ) or standard diet (Altromin, #1314, Lage, Germany) for 1-16 wk. Mice were maintained group-housed on a 12h/12h light dark cycle at 25°C under specific pathogen free (SPF) conditions. C57BL/6-Tg(Foxp3-DTR/EGFP)23.2Spar/Mmjax mice, referred to as Foxp3 DTR mice, were kindly provided by Tobias Bopp (Institute of Immunology, University Medical Center Mainz, Johannes Gutenberg-University, Mainz, Germany) and Stat6KO 4get-GFP BALB/c mice (Gessner et al., 2005) were

kindly provided by Benno Weigmann (Department of Medicine 1, University of Erlangen-Nuremberg, Erlangen, Germany). All mice had *ad libitum* access to food and water and were maintained in the respective animal facilities according to guidelines established by the relevant Institutional Animal Committees. Mice were randomized to test groups. For *in vivo* ADRB3 stimulation or inhibition mice were injected *i.p.* with 1 mg/kg CL or 0.3 mg/kg Cyanopindolol on three consecutive days, respectively. 0.9% NaCl was used as vehicle control. For Treg depletion, Foxp3-DTR mice were injected *i.p.* with 50 ng diphtheria toxin per g bodyweight on three consecutive days. For a second approach of Treg depletion, 250 μg anti-mCD25 antibodies (BioXCell) were injected *i.p.* on three consecutive days (Setiady et al., 2010). For *in vivo* Treg expansion, 6 μg anti-IL2/IL2 antibody (IL-2-mAb) complexes were injected *s.c.* on three consecutive days (Webster et al., 2009). For *in vivo* cold exposure experiments, mice were acclimated to 8°C for 1 wk or to 4°C for 24 h as indicated in the text. No animals were excluded due to illness or outlier results; therefore, no exclusion determination was required. The investigators were not blinded to group allocation or to the assessment of experimental end points. All animal care was executed according to guidelines established by the Institutional Animal Committees at each institution. Ethical approval for all mouse experimentations has been received by corresponding local animal welfare authorities (District government of upper Bavaria or Veterinary office of Zurich).

In Vitro Studies with Primary Murine T Cells

Freshly isolated murine $CD4^+$ T cells were cultured for three days in RPMI media (Gibco by life technologies) supplemented with 10% FCS, 1 mM sodium pyruvate (Sigma Aldrich), 50 mM β-mercaptoethanol (Amimed), 1X non-essential amino acids (Merck Millipore), 100 U/ml human recombinant IL-2 (ReproTech), 100 U/ml penicillin and 100 μg/ml streptomycin (Sigma Aldrich) at 37°C in an humidified CO_2 incubator. Cell culture treated 96-well U bottom plates were used (Bio-Greiner one).

METHOD DETAILS

Isolation of $CD4^+$T Cells from Lymphoid Organs

Lymph nodes and spleens were mashed through 70 μm cell strainers in $HBSS^+$ (supplemented with 5% FCS and 10 mM HEPES). After surface antibody staining, $CD4^+$T cells were enriched using biotin-labelled anti-CD4 antibodies and magnetic activated cell sorting (MACS, Miltenyi) with streptavidin microbeads (Miltenyi). Streptavidin-fluorochrome-conjugates (molecular probes by life technologies) were added after 5 min to allow flow cytometric detection. Cells were further processed for FACS sorting as described below. For immunefluorescence experiments, T cells were isolated from lymph nodes using Dynabeads untouched Mouse CD4 Kit (Invitrogen) according to manufacturer's instructions.

Isolation of $CD4^+$T Cells from Adipose Tissues

White adipose tissue was collected in PBS supplemented with 0.5% BSA and digested with Collagenase II solution [3-4 mg/ml Collagenase II, 10 mM $CaCl_2$] for 10 minutes at 37°C on a rotator. The cell suspension was passed through a 200 μm nylon mesh and centrifuged (380xg, 5 min., 4°C) to separate the stromal vascular fraction from adipocytes. Pelleted cells were re-suspended in $HBSS^+$ (HBSS supplemented with 5% FCS and 10 mM HEPES) and stained for flow cytometric analysis. *Brown AT* was digested in three digestion rounds with 1 mg/ml Collagenase D in $HBSS^+$ at 37°C for 20 min on a rotator. Cell suspensions were passed through a 200 μm nylon mesh and stained for flow cytometric analysis.

Cell Staining for Flow Cytometry

Murine FACS Stainings

The following monoclonal antibodies were used for murine FACS stainings: From BioLegend (San Diego, CA): anti-CD4 Biotin (GK1.5, 1:400), anti-CD8a Pacific Blue (53-6.7; 1:300), anti-CD11b Pacific Blue (M1/70, 1:300), anti-CD11c Brilliant Violett 421 (N418, 1:400), anti-B220 Pacific Blue (RA3-6B2, 1:300), anti-F4/80 Pacific Blue (BM8, 1:400), anti-CD25 PerCP-Cy5.5 (PC61, 1:200), anti-CD44 PE (IM7, 1:800, 1:3000 for analysis with ≤1,000 cells per well), anti-Ki67 APC (16A8, 1:400); anti-Ki67 Brilliant Violett 605 (16A8, 1:400), anti-CD90.1 PerCP-Cy5.5 (OX-7, 1:500), anti-CD90.2 APC-Cy7 (30-H12, 1:500); from eBioscience (San Diego, CA): anti-CD4 Alexa Fluor 700 (RM4-5; 1:200; 1:600 for analysis with ≤1,000 cells), anti-CD62L APC (MEL-14, 1:400), anti-Foxp3 FITC (FJK-16s, 1:200), polyclonal donkey anti-rabbit IgG PE (1:2000); from BD Biosciences: anti-CD14 V450 (rmC5-3, 1:400). Unspecific binding of antibodies was prevented by incubation of cell suspensions with Fc-Block (BD Pharmingen, 2.4G2, 1:100) for 10 min on ice, followed by flow cytometric staining for 30 min on ice in the dark. Cells were passed through a 40 μm cell strainer (NeoLab) to remove large debris. Enumeration of cells and acquisition were performed by using FACSAriaIII and FACSDiva software (BD version 6.1.3). Single-cell data analyses were performed by the use of the FlowJo software 7.6.1 (Tree Star, OR).

Intracellular Staining

To detect intracellular protein expression, T cells were fixed and permeabilized using the Foxp3 Staining Buffer Set (eBioscience) after surface staining. For phospho-Stat6 stainings, MACS-enriched $CD4^+$ T cells were cultured over night with 5 μg/ml plate-bound anti-CD3 and anti-CD28 in RPMI media with supplements and 100 U/ml IL-2. Cells were washed and re-stimulated with CL (100 nM) for 15 min. Surface staining was performed as described above with Fc Block supplemented with sodium vanadate (New England Biolabs). Cells were fixed with PFA (4.5% Histofix, Carl Roth) and permeabilized with 100% methanol. Anti-phospho Stat6-AlexaFluor 647 was stained as recommended by the manufacturer.

Sample Acquisition

Cells were acquired on BD FACSAriaIII flow cytometer using FACSDiva software with optimal compensation and gain settings determined for each experiment based on unstained and single-color stained samples. Doublets were excluded based on SSC-A vs. SSC-W plots and FSC-A vs. FSC-W plots. Live cell populations were gated on the basis of cell side and forward scatter and the exclusion of cells positive for Sytox Blue (Life Technologies) or Fixable Viability Dye eFluor450 (eBioscience). Samples were analyzed using FlowJo software version 7.6.1 (TreeStar, OR).

In vitro Treg-Induction Assay

Murine naive $CD4^+$T cells were defined as $CD4^+CD25^-Foxp3^-GFP^-CD44^{low}$ for Foxp3-GFP reporter mice and as $CD4^+CD25^-CD44^{low}$ for non-reporter mice. Cells were sorted with a FACSAriaIII (BD) cell sorter for purity. Murine naive $CD4^+$T cells were cultured for 18 hours in RPMI media (Gibco by life technologies) supplemented with 10% FCS, 1 mM sodium pyruvate (Sigma Aldrich), 50 mM β-mercaptoethanol (Amimed), 1X non-essential amino acids (Merck Millipore), 100 U/ml human recombinant IL-2 (ReproTech), 100 U/ml penicillin and 100 μg/ml streptomycin (Sigma Aldrich) in 96-well plates pre-coated with 5 μg/ml anti-CD3e (145-2C11, BD Pharmingen) and 5 μg/ml anti-CD28 (37.51, BD Pharmingen). TCR stimulation was limited to 18 hours by transferring cells into uncoated wells. Cells were cultured for additional 36 hours without further TCR stimulation.

Chemicals and Enzymes Used for Experiments

To test the influence of adrenergic receptor stimulation or inhibition on Treg induction capacities, chemicals were added to *in vitro* cultures in the concentrations given in the text: CL-316243 (Sigma Aldrich, CAS 138908-40-4) and Cyanopindolol hemifumarate (Tocris, CAS 69906-86-1). To evaluate the influence of specific signaling pathways on Treg induction we used a specific PTEN inhibitor SF1670 (Abcam, CAS 345630-40-2) and a specific Stat6 inhibitor AS 1517499 (Axon Medchem, CAS 919486-40-1). Collagenase type II (Sigma Aldrich, EC #3.4.24.3) and Collagenase D (Roche, EC #3.4.24.3) were used for T cell isolation from ATs.

Quantitative Analysis of mRNA Abundance

RNA Extraction and cDNA Synthesis

Total RNA was extracted from sort-purified T cell populations using QIAzol Lysis Reagent/ miRNeasy Micro Kit and from snap-frozen total tissue samples (BAT, scWAT, visWAT), which were previously homogenized using QIAshredder (Qiagen) according to the manufacturer's instructions. 1 μg total RNA was converted to first strand cDNA using iScript Advanced cDNA Synthesis Kit (Bio-Rad). For cell numbers < 2000 and/or RNA amounts < 200 ng, cDNA synthesis and subsequent amplification was performed using the SMARTer ultra-low input RNA Kit for sequencing – v4 or SMARTer Universal Low Input RNA Kit for Sequencing (Takara Clonetech) according to the manufacturer's instructions. cDNA was generated in the Thermal Cycler peqStar 2X (Peqlab). Real-time PCR quantification was performed using SsoFast Evagreen Supermix (Bio-Rad) or SYBR Premix Ex Taq (Takara Clonetech) and gene-specific primer sets on a CFX96 real time system (Bio-Rad). *Histone* and *18S* RNA levels were used for normalization of target gene expression levels. Analysis of candidate genes involved in thermogenesis, browning, lipolysis, glycolysis and inflammation was performed. *Primers* used for Quantitative Real-Time PCR analyses are listed in Table S1.

Gel Electrophoresis

2% (w/v) peqGOLD Universal Agarose (Peqlab) was dissolved in 1X TAE Buffer (Applichem) and 3 μL/100 mL Midori Green Advance (Biozym Scientific) were added. Products from RT-qPCR were mixed with Gel Loading Dye Blue (BioLabs). 100 bp Ladder (New England Biolabs) was used as reference. Gel electrophoresis was performed with 130 V for 40-120 min using the power supply unit peqPOWER E250 (Peqlab). DNA fragments were detected using FUSION-FX7 Spectra (Vilber).

mRNA Expression Profiling

cDNA Synthesis: cDNA was generated directly from cells in the Thermal Cycler peqStar 2X (Peqlab) using the SMARTer ultra-low input RNA Kit for sequencing – v4 or SMARTer Universal Low Input RNA Kit for Sequencing (Takara Clonetech) according to the manufacturer's instructions. mRNA expression profiling using next generation sequencing (NGS). For NGS, cDNA concentration and integrity (quality) of the samples were assessed using Agilent High Sensitivity DNA Chips (Agilent Technologies) and Agilent 2100 Bioanalyzer. We employed NGS for expression profiling in pooled sample-sets of $CD4^+$T cells purified from white and brown fat. mRNA library preparation was conducted with Nextera reagents (Illumina), according to the manufacturer's instructions. NGS was performed on a NextSeq (Illumina) with 75bp single end reads for mRNA using Illumina reagents and following the manufacturer's instructions.

NGS Data Processing and Statistical Analysis

Quality was assessed by FastQC (Andrews, 2010). Reads were mapped to the mouse genome (mm10) using BWA-mem with default configuration. Read counts lists were created using SAMTools (Li et al., 2009) and HTSeq-count (Anders et al., 2015). Reads were normalized using DESeq2 (Love et al., 2014). Normalized read counts were further processed for descriptive visualization of expression trends for this preliminary experiment. The cut-off for reading counts was set to 30 and pseudogenes were manually removed. The top 5 upregulated genes are shown.

Proteomics

Mice were treated for three days with 1 mg/kg CL316243 or 0.9% NaCl as vehicle control *in vivo*. Additionally, mice were subjected to cold exposure (8°C) vs. room temperature for 1 week $CD4^+$T cells were isolated by MACS enrichment using CD4-biotin antibodies and streptavidin microbeads as described above.

Sample Preparation for LC-MS/MS Analysis

Cell lysis of isolated cells was performed in LB buffer (50% (v/v) 2-2-2-trifluoroethanol (TFE) plus 2 mM dithiothreitol, 50% (v/v) 50 mM ammonium bicarbonate (ABC) buffer) at 99°C for 10 min followed by sonication for 10 min (10 cycles high intensity, Bioruptor, Diagenode). Cell debris was removed after 10 min centrifugation (16,000 g at 4°C) and proteins in the lysate were alkylated for 30 min with 10 mM iodoacetamide in the dark. Next, the solution was centrifuged in a vacuum evaporator for about three hours at 45°C. Proteins were resolubilized in 10% (v/v) TFE in 50 mM ABC and sonicated in a water bath for 5 min. Proteins were digested by adding 0.2 μg of LysC and 0.2 μg of Trypsin and incubation at 37°C overnight. The next day, the digest was stopped by adding 1% (v/v) TFE and the solution volume was reduced in a vacuum evaporator for about one hour at 45°C. Samples were finally desalted on SDB-RPS StageTips (3M, Empore, Neuss, Germany) and eluted as described (Kulak et al., 2014).

LC-MS/MS Analysis

MS analysis was performed using Q-Exactive HF mass spectrometers (Thermo Fisher Scientific, Bremen, Germany) coupled on-line to a nanoflow UHPLC instrument (Easy nLC, Thermo Fisher Scientific). Peptides were separated on a 50 cm long (75 μm inner diameter) column packed in-house with ReproSil-Pur C18-AQ 1.9 μm resin (Dr. Maisch GmbH, Ammerbuch, Germany). Column temperature was kept at 50 °C by an in-house designed oven with a Peltier element and operational parameters were monitored in real time by the SprayQc software (Scheltema and Mann, 2012). Peptides were loaded with buffer A (0.1% (v/v) formic acid) and eluted with a nonlinear gradient of 5–60% buffer B (0.1% (v/v) formic acid, 80% (v/v) acetonitrile) at a flow rate of 300 nl/min. Peptide separation was achieved by 120 min gradients. The survey scans (300–1650 m/z, target value = 3E6, maximum ion injection times = 20ms) were acquired at a resolution of 60,000 followed by higher-energy collisional dissociation (HCD) based fragmentation (normalized collision energy = 27) of up to 15 dynamically chosen, most abundant precursor ions (isolation window = 1.4 m/z). The MS/MS scans were acquired at a resolution of 15,000 (target value = 1E5, maximum ion injection times = 60 ms). Repeated sequencing of peptides was minimized by excluding the selected peptide candidates for 20 s.

Computational MS Data Analysis

All data was analyzed using the MaxQuant software package 1.5.3.29 (Cox and Mann, 2008). The false discovery rate (FDR) cut-off was set to 1% for protein and peptide spectrum matches. Peptides were required to have a minimum length of 7 amino acids and a maximum mass of 4600 Da. MaxQuant was used to score fragmentation scans for identification based on a search with an initial allowed mass deviation of the precursor ion of a maximum of 4.5 ppm after time-dependent mass calibration. The allowed fragment mass deviation was 20 ppm. Fragmentation spectra were identified using the UniprotKB *Mus musculus* database (UniProt, 2015), based on the 2014_07 release, combined with 262 common contaminants by the integrated Andromeda search engine (Cox et al., 2011). Enzyme specificity was set as C-terminal to arginine and lysine, also allowing cleavage before proline, and a maximum of two missed cleavages. Carbamidomethylation of cysteine was set as fixed modification and N-terminal protein acetylation as well as methionine oxidation as variable modifications. Both 'label-free quantification (MaxLFQ)' and 'match between runs' with standard settings were enabled (Cox et al., 2014). Protein copy number estimates were calculated using the iBAQ algorithm (Schwanhäusser et al., 2011).

Statistics and Data Visualization

Basic data handling, normalization, statistics and annotation enrichment analysis was performed with the Perseus software package (Tyanova, 2016). We filtered for protein groups that were quantified with at least two valid values in at least one group of triplicates. Missing values were imputed with values representing a normal distribution (generated at 1.8 standard deviations of the total intensity distribution, subtracted from the mean, and a width of 0.3 standard deviations). Differentially expressed proteins were identified by one-way ANOVA test at a permutation-based FDR cutoff of 0.05. Enrichment for annotation categories was evaluated by 1D annotation enrichment or Fisher exact test to obtain a p-value. The mass spectrometry proteomics data have been deposited to the ProteomeXchange Consortium (Vizcaino et al., 2014) via the PRIDE partner repository with the dataset identifier ProteomeX change: PXD004671.

Immunefluorescence by Confocal Microscopy

T cells were isolated from thymus and lymph nodes with Dynabeads untouched $CD4^+$ mouse kit (Invitrogen) according to the manufacturer's instructions. Isolated cells were fixed with PFA (Histofix 4.5%, Carl Roth) for 10 min at RT. Immunefluorescence staining was done using rat-anti-mCD4 antibodies (RM4-5; BioLegend) and goat-anti-rat antibodies conjugated with AlexaFluor488 dye (Life Technologies). For CD3 staining armenian hamster-anti-mouse antibodies (145-2C11; BioLegend) were used together with biotinylated goat-anti-hamster antibodies followed by streptavidin-AlexaFluor488 (Life Technologies). For mTOR immunefluorescence analyses, mouse-anti-mTOR antibodies (215Q18; Thermo) and donkey-anti-mouse antibodies conjugated with AlexaFluor555 (Life Technologies) were used. For CD107b staining rat-anti-mouse LAMP2 (M3/84; BioLegend) antibodies were used followed by goat-anti-rat antibodies conjugated with AlexaFluor488 dye (Life Technologies). STAT6 was stained using mouse-anti-mSTAT6 antibodies followed by goat-anti-mouse antibodies conjugated with Cy3 dye. Negative control slides were incubated with secondary antibodies only. In most experiments the cells were PFA-fixed and prepared with cytospin centrifuge (Shandon). For Foxp3 staining, T cells were aceton-fixed, incubated with rat-anti-mouse antibodies (eBioscience) and goat-anti-rat antibodies conjugated with AlexaFluor594

dye (BioLegend). Nuclei were counterstained with DAPI (Vector). Finally, cells were analyzed by confocal microscopy (Leica DMI6000CS).

Immunofluorescence by STED Microscopy

Untouched $CD4^+$T cells from inLNs were fixed with PFA for 10 min at RT. After permeabilization with TritonX100 for 5 min and protein block for 10 min with 2% BSA, staining of rat anti-CD4 antibody (BD) and rabbit anti-C17orf59 antibody (MyBioSource) was performed. Goat-anti-rat-STAR580 (abberior) and goat-anti-rabbit STAR635P (abberior) were used as secondary antibodies. Finally, nuclei were counterstained with DAPI. Negative control slides were incubated with secondary antibodies only. Cells were analyzed by Abberior 3D STED 2-Channel Super Resolution Microscope (Abberior, Göttingen). The dye STAR580 was excited with a 594 nm pulsed laser, STAR635p with a 640 nm pulsed laser and DAPI with a 405 nm CW laser and depletion of STAR580 + STAR635p was done with a 775 nm pulsed STED laser.

QUANTIFICATION AND STATISTICAL ANALYSIS

Results are presented as means±SEM, as percentage, where appropriate or as summary box-and-whisker plots indicating minimum to maximum values to demonstrate data distribution. For normally distributed data, Student's t-test for unpaired values was used to compare independent groups. Group size estimations were based upon a power calculation to minimally yield an 80% chance to detect a significant difference in the respective parameter of $p<0.05$ between the relevant groups. For all tests, a two-tailed p value of <0.05 was considered to be significant. Statistical significance is shown as * = $p<0.05$; ** = $p<0.01$; *** = $p<0.001$. N numbers can be found within the text and/or within the figure legends. Analyses were performed using GraphPad Prism 6.0.1 (La Jolla, CA) and the Statistical Package for the Social Sciences (SPSS 19.0; SPSS, Chicago, IL).

DATA AND SOFTWARE AVAILABILITY

Data Resources

The mass spectrometry proteomics data have been deposited to the ProteomeXchange Consortium (Vizcaino et al., 2014) via the PRIDE partner repository with the dataset identifier ProteomeXchange: PXD004671.